AGU PUBLICATIONS

JGR

Journal of Geophysical Research: Space Physics

RESEARCH ARTICLE
10.1002/2014JA020792

Key Points:
- Energetic electron events measured with MESSENGER's Gamma-Ray and Neutron Spectrometer
- The electron events form quasi-permanent structures in Mercury's magnetosphere
- Some events show periodicities from hundreds of seconds to tens of milliseconds

Correspondence to:
D. J. Lawrence,
David.J.Lawrence@jhuapl.edu

Citation:
Lawrence, D. J., et al. (2015), Comprehensive survey of energetic electron events in Mercury's magnetosphere with data from the MESSENGER Gamma-Ray and Neutron Spectrometer, *J. Geophys. Res. Space Physics*, *120*, 2851–2876, doi:10.1002/2014JA020792.

Received 5 NOV 2014
Accepted 25 FEB 2015
Accepted article online 28 FEB 2015
Published online 27 APR 2015

Comprehensive survey of energetic electron events in Mercury's magnetosphere with data from the MESSENGER Gamma-Ray and Neutron Spectrometer

David J. Lawrence[1], Brian J. Anderson[1], Daniel N. Baker[2], William C. Feldman[3], George C. Ho[1], Haje Korth[1], Ralph L. McNutt Jr.[1], Patrick N. Peplowski[1], Sean C. Solomon[4,5], Richard D. Starr[6], Jon D. Vandegriff[1], and Reka M. Winslow[7,8]

[1]The Johns Hopkins University Applied Physics Laboratory, Laurel, Maryland, USA, [2]Laboratory for Atmospheric and Space Physics, University of Colorado Boulder, Boulder, Colorado, USA, [3]Planetary Science Institute, Tucson, Arizona, USA, [4]Department of Terrestrial Magnetism, Carnegie Institution of Washington, Washington, District of Columbia, USA, [5]Lamont-Doherty Earth Observatory, Columbia University, Palisades, New York, USA, [6]Physics Department, Catholic University of America, Washington, District of Columbia, USA, [7]Department of Earth, Ocean and Atmospheric Sciences, University of British Columbia, Vancouver, British Columbia, Canada, [8]Institute for the Study of Earth, Oceans, and Space, University of New Hampshire, Durham, New Hampshire, USA

Abstract Data from the MErcury Surface, Space ENvironment, GEochemistry, and Ranging (MESSENGER) Gamma-Ray and Neutron Spectrometer have been used to detect and characterize energetic electron (EE) events in Mercury's magnetosphere. This instrument detects EE events indirectly via bremsstrahlung photons that are emitted when instrument and spacecraft materials stop electrons having energies of tens to hundreds of keV. From Neutron Spectrometer data taken between 18 March 2011 and 31 December 2013 we have identified 2711 EE events. EE event amplitudes versus energy are distributed as a power law and have a dynamic range of a factor of 400. The duration of the EE events ranges from tens of seconds to nearly 20 min. EE events may be classified as bursty (large variation with time over an event) or smooth (small variation). Almost all EE events are detected inside Mercury's magnetosphere on closed field lines. The precise occurrence times of EE events are stochastic, but the events are located in well-defined regions with clear boundaries that persist in time and form what we call "quasi-permanent structures." Bursty events occur closer to dawn and at higher latitudes than smooth events, which are seen near noon-to-dusk local times at lower latitudes. A subset of EE events shows strong periodicities that range from hundreds of seconds to tens of milliseconds. The few-minute periodicities are consistent with the Dungey cycle timescale for the magnetosphere and the occurrence of substorm events in Mercury's magnetotail region. Shorter periods may be related to phenomena such as north-south bounce processes for the energetic electrons.

1. Introduction

Since the Mariner 10 flybys of Mercury, it has been known that transient bursts of energetic particles, specifically energetic electron (EE) events, are produced in Mercury's magnetosphere [*Simpson et al.*, 1974; *Eraker and Simpson*, 1986]. The Mariner 10 observations not only demonstrated the existence of these bursts, they also provided evidence for high electron energies (hundreds of keV) and showed that some of these events had coherent time periodicities of ~5 to 6 s [*Simpson et al.*, 1974; *Eraker and Simpson*, 1986]. Subsequent interpretations of Mariner 10 data [*Baker et al.*, 1986; *Christon et al.*, 1987] placed these bursts into the context of "substorm" processes common in Earth's magnetosphere [*Baker et al.*, 1996]. Further analyses [*Baker et al.*, 1987] treated questions about auroral zones and radiation belts in Mercury's magnetosphere. *Ho et al.* [2011a] confirmed the occurrence of these energetic particle events and described some of their characteristics with data from the MErcury Surface, Space ENvironment, GEochemistry, and Ranging (MESSENGER) spacecraft [*Solomon et al.*, 2007], particularly from MESSENGER's Energetic Particle Spectrometer (EPS) and also from the spacecraft's X-Ray Spectrometer (XRS) and Neutron Spectrometer (NS). In a subsequent study, *Ho et al.* [2012] included observations from the full year of MESSENGER's primary orbital mission phase and reported the spatial distribution of 51 EE events. These studies demonstrated that the electrons in these events have energies up to hundreds of keV and are widely distributed in latitude and local time and that stable, long-lived

Van-Allen-type radiation belts are not present at Mercury. Finally, when *Sundberg et al.* [2012] studied dipolarization events at Mercury, they did not find any particle energization from either the EPS or XRS as reported by *Christon et al.* [1987] from the Mariner 10 data set. It is worth noting that *Simpson et al.* [1974] claimed to have detected energetic (>550 keV) protons as well as energetic electrons. However, it was suggested soon afterward that the signals identified as proton detections may instead have resulted from the pileup of lower-energy (<170 keV) electrons [*Armstrong et al.*, 1975]. The initial reports of the detection of energetic electrons with MESSENGER data [*Ho et al.*, 2011a, 2011b, 2012] discussed these disparate interpretations of Mariner 10 data and showed that the primary energetic particles within Mercury's magnetosphere are electrons, not protons.

In this study, we build on these earlier results with a comprehensive survey of EE events measured with the MESSENGER NS, supplemented with observations from MESSENGER's Gamma-Ray Spectrometer (GRS). Both the NS and the GRS are sensors on MESSENGER's Gamma-Ray and Neutron Spectrometer (GRNS) instrument [*Goldsten et al.*, 2007]. Although the primary purpose of the NS and GRS is to apply neutron and gamma-ray spectroscopy to the characterization of Mercury's surface composition [e.g., *Peplowski et al.*, 2011; *Lawrence et al.*, 2013], both instruments are sensitive to bremsstrahlung photons produced when energetic electrons impact materials near the neutron and gamma-ray sensors. The NS and GRS provide several advantages for EE event detection and characterization compared with the EPS. First, the NS and GRS each have detector areas more than two orders of magnitude larger than that of the EPS [*Goldsten et al.*, 2007; *Andrews et al.*, 2007]. This increased sensitivity is illustrated by the fact that during the same time period in which the EPS detected 51 EE events [*Ho et al.*, 2012], the NS detected 733 EE events (see below, section 6). Second, both the NS and GRS have higher time resolution than the EPS. Specifically, the NS has a 1-s burst-mode capability that is able to resolve the time variability of EE events with a factor of 3 improvement over that of the EPS [*Ho et al.*, 2011a]. The flight software readout of the anticoincidence shield (ACS) on the GRS was upgraded in early 2013 to allow characterization of EE events at 10 ms resolution. These capabilities enable the temporal variation of EE events to be well characterized over a wide range of accumulation times.

The survey of EE events at Mercury in this paper was conducted with 30 months of continuously recorded NS data. After describing the instrumentation used to make the measurements (section 2), we present examples of EE events and discuss quantitative evidence for their identification (section 3). We then describe the analysis procedure used to isolate the EE events from the NS data (section 4). In section 5, we present evidence that EE events can be classified on the basis of intrinsic event parameters. We further describe the systematic behavior of EE event parameters (e.g., size, duration, and time variation) and show how these parameters vary with other observational measurables such as latitude, altitude, local time, and magnetic field. In section 6, we compare and contrast the NS-measured EE events with those measured by the EPS and XRS. From the accumulated data, we draw inferences regarding event generation scenarios and what these events reveal about Mercury's magnetosphere, and we conclude with questions for future studies.

2. MESSENGER's Gamma-Ray and Neutron Spectrometer

Full descriptions of the MESSENGER GRNS and the use of the GRS and NS sensors in the MESSENGER mission have been given by *Goldsten et al.* [2007], *Feldman et al.* [2010], *Peplowski et al.* [2011, 2012], and *Lawrence et al.* [2013]. Several aspects of the design and operation of the sensors are relevant to the present study. Specifically, the NS and GRS are sensitive to bremsstrahlung photons that are produced by energetic electrons that hit materials located near the respective sensors (see section 3.2).

The NS consists of three scintillator sensors read out by separate photomultiplier tubes [*Goldsten et al.*, 2007]. The NS is located on the side of the MESSENGER spacecraft opposite to the spacecraft's sunshade, which always points within 10° of the sunward direction [*Leary et al.*, 2007]. The NS has operated nearly continuously since MESSENGER was inserted into its eccentric orbit about Mercury on 18 March 2011. The central NS sensor is a $10 \times 10 \times 10\ cm^3$ cube of borated plastic (BP) scintillator (Bicron BC454). Because of its large volume, the BP sensor has high sensitivity to EE events, and data from this sensor provide the primary NS-based EE event data set. The NS operates in three modes: near planet, far planet, and burst. When MESSENGER is near Mercury, defined by an altitude h less than 7000 km, the NS accumulates data with a time cadence of 20 s. When MESSENGER is far from Mercury ($h > 7000$ km), the NS accumulates data with a time cadence of 300 s. The near-planet accumulation time is sufficiently short to provide high sensitivity for EE event detection, but the

far-planet accumulation time is too long to allow detection. On the basis of identified event locations, the vast majority of all EE events are observed at altitudes less than 7000 km (section 5.2). There is therefore little loss of EE event detection sensitivity when the NS operates in its 300-s accumulation mode.

In its burst mode, the NS autonomously detects large (four standard deviation) enhancements in the BP count rate with 1-s accumulations across a 164-s moving average [*Goldsten et al*., 2007]. When a burst is detected, the returned data consist of the total BP count rate in a 164-s interval with 1-s time resolution; the first 34-s of this interval contain pretrigger data. The original purpose of the NS burst mode was to detect galactic gamma-ray bursts to help constrain burst positions using data from widely separated spacecraft [e.g., *Mazets et al*., 2008]. However, Mercury EE events vary over timescales comparable to the cadence of the NS burst mode, so the NS burst observations provide a valuable data subset with a time resolution (1 s) that is a factor of three shorter than that for EPS data (3 s). For the nominal BP data (not NS burst mode), scintillator energy deposition information is returned for each 20-s or 300-s accumulation period. Specifically, the BP energy spectra are divided into 64 channels with an energy-deposition threshold of 20–40 keV.

The GRS contains two sensors: a cooled, high-purity Ge (HPGe) gamma-ray sensor sensitive to gamma rays from 50 keV to 10 MeV, and a borated plastic (Bicron BC454) anticoincidence shield (ACS) designed to actively reject background charged particles from the Ge gamma-ray measurements. The GRS is located near the spacecraft adapter ring and has a field of view boresighted with MESSENGER's optical instruments [*Leary et al*., 2007]. Because the HPGe sensor requires cryogenic cooling to operate at temperatures less than 100 K, the GRS includes a miniature, limited-life cryocooler (Ricor K508). The cooler stopped operating on 15 June 2012 after having accumulated over ~9500 h of operation. The EE event data from the HPGe sensor are available near-continuously from 18 March 2011 to 11 October 2011 and intermittently from 12 October 2011 until the cryocooler failure. The ACS has operated near-continuously since orbit insertion on 18 March 2011.

When the cryocooler was operating, the GRS had two operational modes: near planet and far planet. For the near-planet mode ($h < 5000$ km), both GRS sensors accumulated data with a time cadence of 60 s. For the far-planet mode ($h > 5000$ km), both sensors accumulated data with a time cadence of 3600 s. Because of these longer time cadences compared with those of the NS, the early GRS data are not as sensitive to the time-dependent EE events as the NS. However, the high-energy-resolution HPGe data provide important constraints on the energy deposition behavior of detected EE events.

After the HPGe cooler stopped operating, the GRS flight software was reconfigured to optimize ACS measurements of EE events and planetary neutrons. Specifically, the memory for the 16,384 channels of the HPGe system was repurposed to provide 10-ms sampling of the total ACS count rates. This memory reconfiguration enabled an improvement by two orders of magnitude in the temporal resolution of EE events compared with that for the NS burst mode and a factor of 60 improvement compared with the 0.6 s resolution of the Mariner 10 measurements [*Simpson et al*., 1974]. In addition, the GRS operating modes were modified to be similar to those of the NS with a near-planet ($h < 4000$ km) time cadence of 20 s. The far-planet time cadence for the reconfigured ACS data is 1800 s. Because of the similarity in the sizes of the NS and ACS borated plastic sensors, these later data provide a similar time-resolved data set and may also provide some directional information on EE events because of the different locations of the NS and the ACS on the MESSENGER spacecraft.

3. Overview of NS and GRS Measurements of EE Events

This section provides an overview of EE events as observed in both the NS and GRS data. We include a summary of time and energy characteristics as well as a detailed justification of why these events seen with the NS and GRS sensors are attributed to energetic electrons.

3.1. EE Events Observed With the NS

EE events were seen in the NS data soon after the MESSENGER spacecraft was inserted into orbit about Mercury. On the basis of 30 months of nearly continuous data, EE events are now known to exhibit a wide variety of magnitudes and time characteristics. A sampling of different NS-measured EE events is shown in Figure 1. The figure shows six different time periods with EE event detections. In each panel, the total BP count rate for the 11 lowest energy-deposition channels is plotted versus time. In each example, the slowly varying count rate that peaks between 30 and 60 min is due to neutrons and downscattered gamma rays from Mercury's surface interacting in the BP sensor [*Lawrence et al*., 2013]. The slowly changing shape of the time profile is the result of

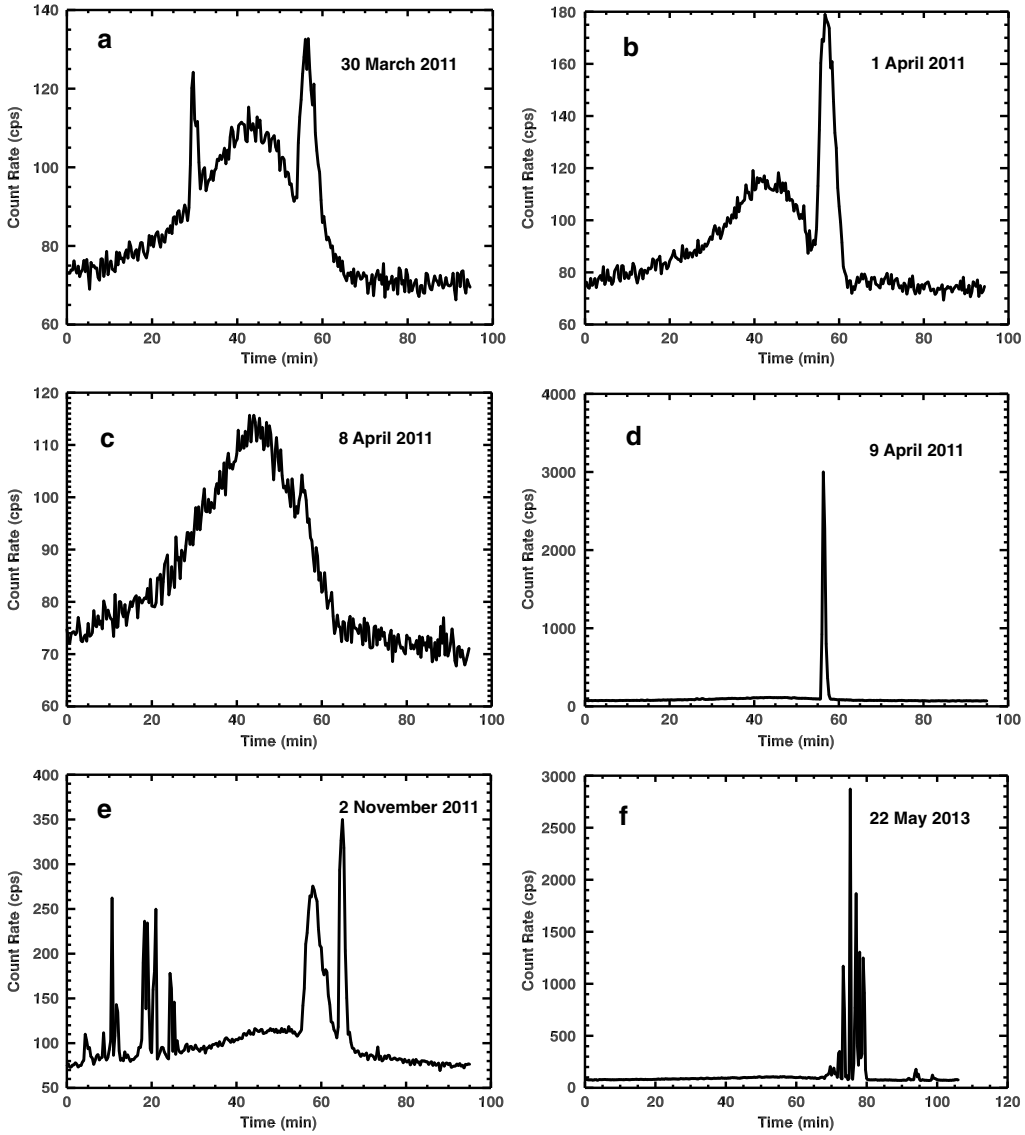

Figure 1. Six examples of energetic electron events measured with the NS. Count rates of the lowest 11 channels (0–10) from the borated plastic singles events in units of counts per second (cps) are plotted versus the time after the spacecraft passed below 4000 km altitude on the incoming portion of a given orbit. (a) 30 March 2011. (b) 1 April 2011. (c) 8 April 2011. (d) 9 April 2011. (e) 2 November 2011. (f) 22 May 2013.

the changing solid angle subtended by Mercury as viewed by the NS and the asymmetric viewing geometry of the body-mounted NS as the MESSENGER spacecraft changed its attitude during periapsis passes. More rapid count-rate changes of varying intensity and time durations are seen superimposed on the slow count-rate variations. These rapid count-rate changes are the energetic electron events. Figures 1a and 1b show typical EE events detected early in MESSENGER's orbital mission phase. Figure 1c shows a small event close to minute 55 near the detection limits. Figure 1d shows one of the largest detected events, which dwarfed the signal originating from Mercury's surface. The time duration of the events ranges from less than 1 min to greater than 15 min, and the event count rates vary by more than a factor of 400. The events exhibit a variety of temporal characteristics ranging from smooth (e.g., Figures 1a and 1b) to "bursty" (e.g., Figure 1f). The term smooth denotes a temporal profile that varies slowly across multiple accumulation periods, and the term bursty denotes events that show large time variability from one accumulation period to the next. Bursty and smooth events can occur closely in time on the same orbit (Figure 1e). A description of how the NS-measured EE events are identified and separated from the "background" neutron measurements is given in section 4. More details about the bursty and smooth classifications are given in section 5.1. We note that the precise occurrence time of the EE events on

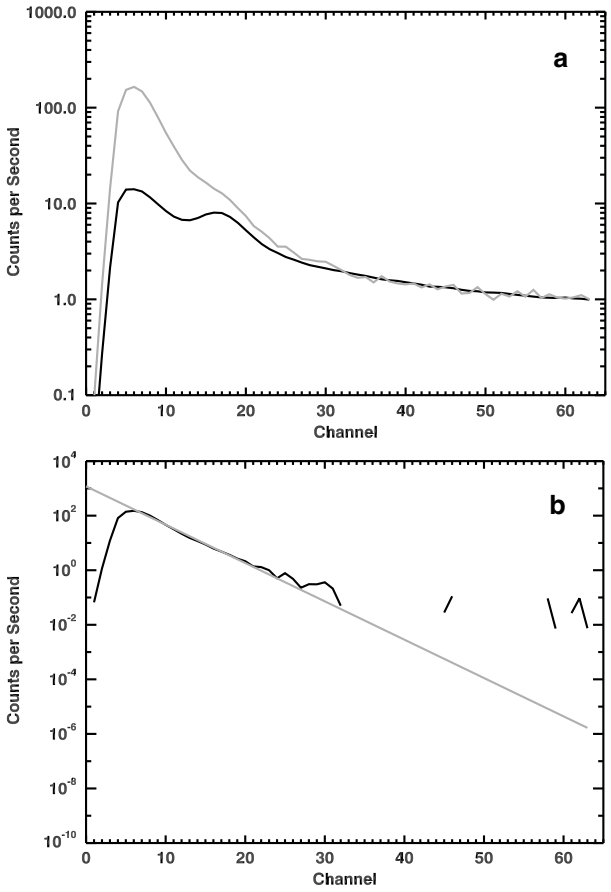

Figure 2. Energy deposition spectra in the borated plastic NS scintillator from the 9 April 2011 EE event. Energy is given in units of pulse height channels, and count-rate is given in units of counts per second. (a) Average count-rate energy spectrum for the EE event (gray trace) and average background spectrum (black) taken from all non-EE-event times on the same day during periods when the spacecraft altitude was less than 7000 km. The peak around channel 17 is due to the 93 keV electron-energy-equivalent deposition of the $^{10}B(n,\alpha)$ reaction triggered by neutrons originating from Mercury. (b) Net EE event spectrum after subtraction of the background spectrum from the EE event spectrum. The gray line shows an exponential fit to the count rate, y, versus channel, x: $y = a\ \exp(x/b)$. The fitted parameters are $a = 1187$ and $b = -3.1$.

an orbit-by-orbit basis is stochastic, and it is not predictable on any given orbit whether an event will be detected.

The energy deposition spectrum for a large EE event (9 April 2011, Figure 1d) is shown in Figure 2, along with the average non-EE-event spectrum for times near Mercury ($h < 7000$ km) on the same orbit. The higher-energy background for channels above 30 is due mostly to Compton-scattered gamma rays depositing energy in the BP sensor. The sharp cutoff below channel 5 is a result of the discriminator threshold in the NS electronics. Figure 2a shows that during the EE event there was a substantial increase in low-energy counts but virtually no change in count rate above channel 30 (or approximately 160 keV electron-energy equivalent). On the basis of an extensive analysis of NS data (including this event), it was found that the optimum channel range for EE event detection includes channels 0 through 11. A difference spectrum, obtained by subtracting the non-EE-event spectrum from the EE event spectrum, is shown in Figure 2b. This difference spectrum is well fit by an exponential function.

An example of NS burst-mode data is shown in Figure 3 for the 1 April 2011 event. As seen, the burst-mode data can reveal high-time-resolution information, if present, that is not observable with the nominal 20-s NS data (see section 5.4 for a more detailed description of burst-mode data).

3.2. EE Events Observed With the GRS: Identification of Energetic Electrons

The MESSENGER GRS gamma-ray sensor operated nearly continuously from 29 March 2011 to 11 October 2011, and periodically thereafter until the failure of the cryocooler on 15 June 2012. Measurements of EE events with the GRS sensor partially overlap those of the NS reported here, including five of the six events shown in Figure 1. The gamma-ray measurements have the benefit of a precise energy calibration and a well-known energy-dependent and incidence-angle-dependent response [*Peplowski et al.*, 2012] that makes them particularly well suited for examining the physical characteristics of the EE events.

The large event of 1 April 2011 (Figures 1b and 3) provides an example with which the energy deposition spectrum measured by the gamma-ray sensor may be investigated. As was done with the NS, we subtracted the spectrum of gamma-ray measurements made immediately before and following the EE event from that of the event (Figure 4b), leaving a residual that is attributed entirely to the EE event (Figure 4a). The spectrum shows a broad distribution that peaks near 60 keV, two narrow peaks at energies of ~75 keV, and a rapidly decreasing count rate that extends to a maximum energy of around 400 keV.

Analyses of EE events from Mariner 10 [*Simpson et al.*, 1974] and earlier MESSENGER observations [*Ho et al.*, 2011a, 2011b] indicated that the particle bursts consist of electrons with energies of ~300 keV or less. The GRS

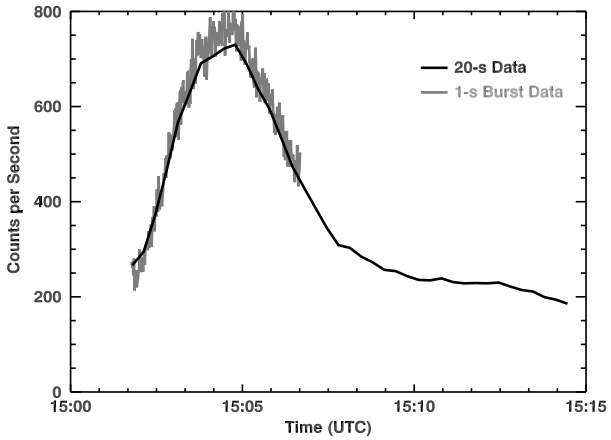

Figure 3. BP singles count rate from the 1 April 2011 EE event from both the 20-s accumulation data (black) and the 1 s burst mode data (gray).

housing is sufficiently thick to stop all electrons with energies less than 500 keV from reaching the gamma-ray sensor, however, so electrons at ≤300 keV energy cannot directly account for the GRS count rates. In order to investigate the source of the measured signal, the radiation transport code Geant4 [*Agostinelli et al.*, 2003] was used to simulate the interactions of energetic electrons with the GRS. The code incorporates a high-fidelity GRS model that was previously shown to reproduce the energy-dependent and incident-angle-dependent response of the instrument to within 5% [*Peplowski et al.*, 2012]. Modeling of electron interactions with the GRS indicates that the electrons produce bremsstrahlung photons as they stop within the GRS housing. These photons are capable of reaching and depositing energy within the gamma-ray sensor. These photons also induce fluorescence in GRS housing materials, including the production of the ~75 keV peaks that correspond to K_α and K_β gold (Au) X-rays. Au is present in coatings that were applied to some surfaces as part of the instrument thermal design [*Burks et al.*, 2004].

Ho et al. [2011b] performed a detailed analysis of EE events as measured by the EPS and XRS during MESSENGER's first two Mercury flybys. They concluded that a kappa function with parameters $K = 8$ and $E_o = 0.7$ keV (see *Ho et al.* [2011b, Table 1] for definition of these parameters) could reproduce the EPS and XRS signals for those events. We extended the Geant4 simulations to include the *Ho et al.* [2011b] electron spectrum and found that it failed to produce any events with gamma-ray energies >100 keV, which sharply contrasts with the GRS-measured spectrum (Figure 4). This result is not surprising, however, as the low relative electron flux at high energies (>100 keV) and soft spectrum are not capable of producing bremsstrahlung gamma rays with energies >100 keV. We therefore conclude that the *Ho et al.* [2011b] kappa function is not consistent with the GRS measurements. Similarly, power-law-shaped spectra with a power law index up to 3 [*Ho et al.*, 2012] are not able to match the measured GRS spectrum. Maxwell-Boltzmann distributions (MBDs), in contrast, successfully reproduced the shape of the measurements. In particular, an MBD with a 90 keV average energy fully matches the GRS observations (Figure 4c). Lower-energy distributions, as illustrated by the MBD with a 30-keV average energy shown in Figure 4c, do not provide a match to the spectrum of the 1 April 2011 event. The match between the 90-keV MBD and the GRS data, along with the production of the 75-keV Au X-rays, shows that GRS

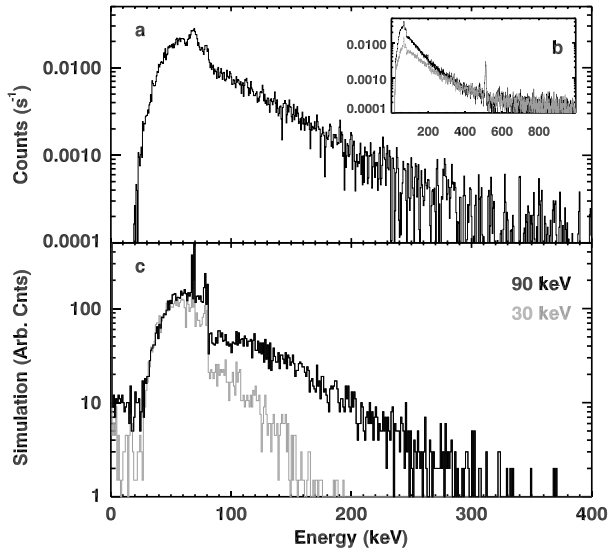

Figure 4. (a) Net energy spectrum of the EE event of 1 April 2011 as recorded in the MESSENGER GRS gamma-ray sensor. (b) The difference spectrum of Figure 4a was derived by subtracting the average spectrum acquired immediately prior to and following the EE event (gray) from the gamma-ray spectrum acquired during the event (black). (c) Geant4 models of EE event-induced signals in the gamma-ray sensor for Maxwell-Boltzmann distributions with an average energy of 90 (black) and 30 keV (gray). The 90 keV distribution produced a good match to the observed spectrum, unlike the 30 keV distribution or the kappa distribution described by *Ho et al.* [2011b].

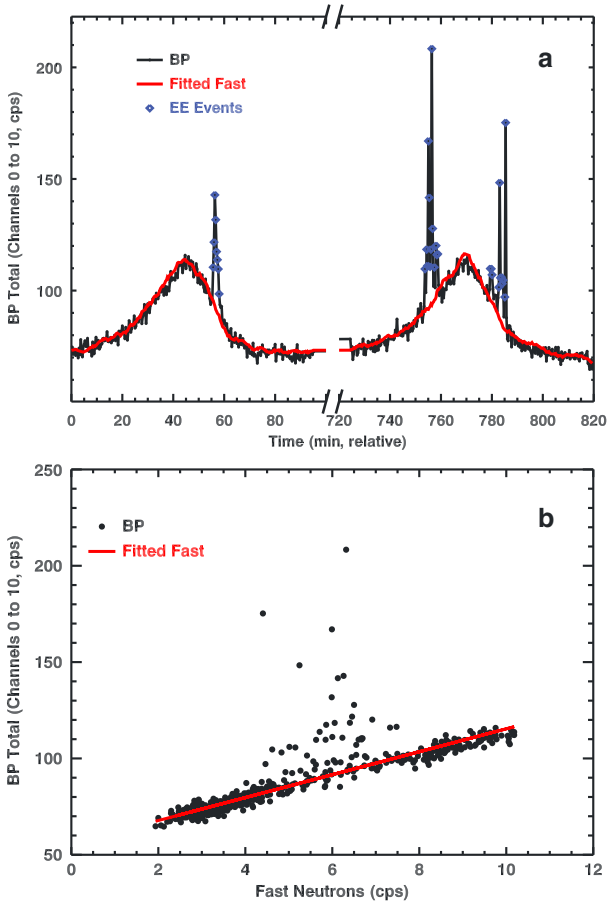

Figure 5. (a) Low-energy count-rate data from the NS BP scintillator on 10 April 2011. The 20-s count rate data are plotted versus time relative to the first inbound crossing of 4000 km altitude for two consecutive orbits (black). Far-planet data with 300-s accumulation times and/or altitudes greater than 4000 km are not included. Fitted fast neutron count rates are shown by the red trace. Blue diamonds show EE events. (b) Fast neutron count rates versus low-energy BP count rates for the time period shown in Figure 5a. The red line shows a linear fit between the two data sets for BP count rates less than 125 cps.

measurements of EE events are attributable to electron-induced bremsstrahlung within the GRS housing. Similar arguments apply to the NS, which includes a comparable housing and detectors that are likewise sensitive to energy deposition by bremsstrahlung photons.

4. Procedure for Identification of Energetic Electron Events With NS Data

We next describe the procedure used to isolate and identify EE events from the low-energy count rates recorded by the NS BP scintillator. Figure 5a shows low-energy BP count-rate data, sampled every 20 s, for 10 April 2011. The two local maxima near 45 min and 140 min are the periapsis passes for the two successive 12-h MESSENGER orbits (far-planet data for this day are not included in Figure 5). EE events are clearly seen as large deviations from the nominal solid-angle dependence of the BP count rate. Figure 5b shows the same low-energy BP count rates, but here plotted versus the measured fast neutron count rate [*Lawrence et al.*, 2013]. The time-domain procedure for isolating fast neutrons in the BP measurements [*Goldsten et al.*, 2007] prohibits contamination of the fast neutron count rate from EE events, making the latter metric a fiducial for Mercury BP scintillator counts originating from Mercury. It is observed from the BP versus fast measurements (Figure 5b) that, except for the EE events, the BP and fast neutron count rates are highly correlated. To reduce scatter from statistical variations, the fast neutron count rate, C_{fast}, has been smoothed in time by a moving 100-s wide boxcar average. The red trace in Figure 5b shows a linear fit of the BP counts, C_{BP}, to the fast neutron count rate for BP values less than 125 counts per second. Here, a fast-neutron-derived, model BP count rate, $C_{BP,model}$, is defined as

$$C_{BP,\,model} = \alpha C_{fast} + b \tag{1}$$

where α and b are constants (Figure 5a). The count rate difference is $C_{diff} = C_{BP} - C_{BP,model}$. To determine a statistically significant EE event signal, the standard deviation, σ_{50th}, of the lower fiftieth percentile BP count rate was determined for the given time base (nominally one orbit). The standard deviation was computed from the lower fiftieth percentile so as not to bias the value with time bins containing EE events. The BP signal-to-noise ratio, $S_{S/N}$, is then $S_{S/N} = C_{diff}/\sigma_{50th}$. Figure 6 shows $S_{S/N}$ for the same time base as that in Figure 5, except that the solid-angle variation of the BP count rate has been removed. Candidate EE events are identified by $S_{S/N}$ values greater than 5 (blue diamonds in Figure 5a). This threshold value of 5 was chosen to be sufficiently large to minimize spurious detections and sufficiently small to provide good EE event detection sensitivity. This threshold is the same as that used to eliminate EE events for planetary neutron analysis [*Lawrence et al.*, 2013].

To complete the EE event identification with a robust algorithm that minimizes false detections but maximizes real events, additional detection criteria have been used. First, it is required that at least two $S_{S/N} > 5$

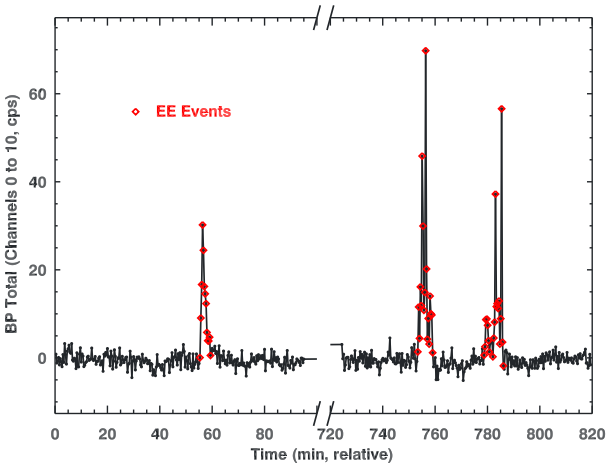

Figure 6. Derived $S_{S/N}$ values versus time for the same time period as that in Figure 5. Identified EE events are shown by the red diamonds.

measurements occur within five 20-s time steps. This requirement reduces spurious single time-step detections and yet allows events with $S_{S/N}$ values at or near the detection limit to be considered as a valid EE event. The time threshold of five 20-s increments was empirically determined to best optimize the identification of contiguous EE events. Second, EE events for a single 20-s time increment are allowed, but only if $S_{S/N} > 9$ in order to reduce spurious detections. Third, after identifying the start and stop times for a period when $S_{S/N} > 5$, the final EE event time boundaries are defined by the times when $S_{S/N}$ drops below 2 at the beginning and end of the event. Figure 6 shows the times of EE events selected on the basis of the above criteria.

During the time period from March 2011 to December 2013, the MESSENGER spacecraft had two orbital periods. From Mercury orbit insertion (18 March 2011) to 16 April 2012, the orbit period was 12 h, the periapsis altitude was a few hundred kilometers, and the apoapsis altitude was ~15,000 km. Since 20 April 2012, the orbit period has been 8 h, the periapsis altitude a few hundred kilometers, and the apoapsis altitude ~10,000 km. Because the MESSENGER spacecraft has sampled different portions of Mercury's magnetosphere in these two types of orbits, we separated the EE event data by the two orbital phases. The total number of EE events detected from the 12-h orbits (NS data from 25 March 2011 to 16 April 2012) is 791. The total number of EE events detected from 8-h orbits through December 2013 (NS data from 22 April 2012 to 31 December 2013) is 1920. The total number of NS-detected EE events from orbit insertion through calendar year 2013 is therefore 2711.

5. Characteristics of NS-Derived EE Events

As shown in Figure 1, EE events have a variety of magnitudes, durations, and time characteristics. In this section, these characteristics are described in greater detail. First, the distinction between "smooth" and "bursty" events is defined. Next, the systematic behavior of event parameters (magnitude, duration, and location) is presented and compared with other MESSENGER spacecraft measurements and derived quantities. Finally, an overview of the time behavior of the events (periodic versus nonperiodic) is described. Except where noted in section 5.4, all results in this section are for NS data acquired with the nominal 20-s accumulation times.

5.1. EE Event Classification

As introduced above, EE events can be classified as being either smooth or bursty, with Figure 1b showing a type example of a smooth event and Figure 1f showing a type example of a bursty event. Since it is expected that such a classification relates to underlying physical processes, we here develop a method to quantify this classification and investigate systematic behavior. To turn the qualitative classification into quantitative categories, we define two parameters that provide a measure of event smoothness. The first parameter is the magnitude-normalized time integral, I_{norm}, and is defined as

$$I_{norm} = \sum_{i=0}^{D} (S_{S/N}) / \max\left[(S_{S/N})_i \right], \tag{2}$$

where the index i denotes an individual time step for a given EE event and D is the event duration in time steps. With this definition, smooth events will have higher values of I_{norm} and bursty events will have lower values of I_{norm}. A second parameter may be derived from the standard deviation of the quotient of the signal-to-noise ratio and a low-pass-filtered ratio:

$$\sigma_{\text{filter ratio}} = \sigma \left(\frac{[S_{S/N}]_i}{B\left[(S_{S/N})_i, w \right]} \right), \tag{3}$$

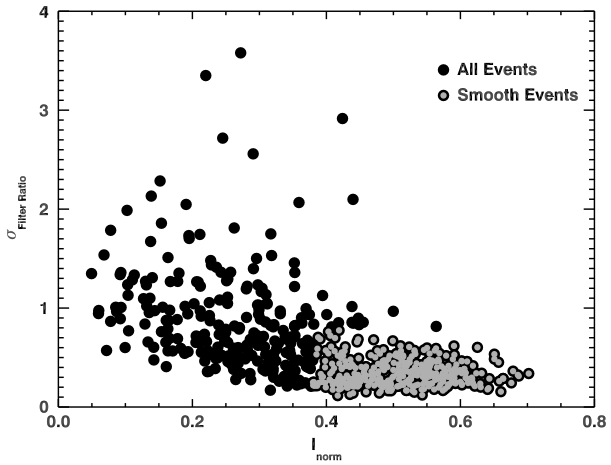

Figure 7. I_{norm} versus $\sigma_{\text{filter ratio}}$ for all EE events from the 12-h orbit mission phase. Gray points show smooth events, defined by I_{norm} values less than 0.38 and $\sigma_{\text{filter ratio}}$ values less than 0.8.

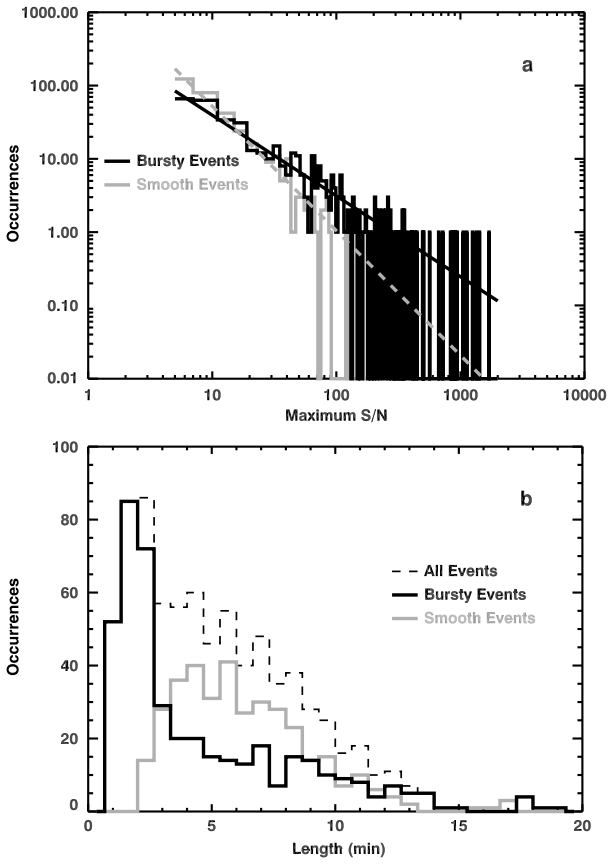

Figure 8. (a) Histograms of maximum $S_{S/N}$ values for EE events from 12-h orbits for smooth events (gray) and bursty events (black). Power laws fit to the two profiles are shown. The scale, a, and power law index, b, respectively, are $a = 498$ and $b = -1.1$ for bursty events and $a = 2618$ and $b = -1.7$ for smooth events. (b) Histograms of EE event durations from the 12-h orbits for smooth events (gray), bursty events (black), and all events (dashed).

where σ is the standard deviation of a time series and $B(x_i,w)$ is a boxcar-shaped smoothing function of values x_i over a moving window of w time steps. The $\sigma_{\text{filter ratio}}$ should have low values for smooth events and high values for bursty events. The value of $w = 3$ was chosen empirically to provide optimum sensitivity of $\sigma_{\text{filter ratio}}$ to an event's smoothness.

A plot of I_{norm} versus $\sigma_{\text{filter ratio}}$ for all events identified from 12-h orbits is shown in Figure 7. A similar variation of values was found for events from 8-h orbits (not shown). The general behavior in Figure 7 shows a moderate anticorrelation of the parameters, with smooth events having higher values of I_{norm} and lower values of $\sigma_{\text{filter ratio}}$. In addition, Figure 7 shows that there is a continuous change from smooth to bursty rather than a sharp delineation between the two end-member event types. Despite this continuous variation, an empirical working definition of smooth versus bursty events can be made, as shown in Figure 7. The distinction between the two types is somewhat arbitrary, because of the continuous change from smooth to bursty, but for the purposes of this study smooth events are defined to have I_{norm} values greater than 0.38 and $\sigma_{\text{filter ratio}}$ values less than 0.8. The next two sections show that this definition of smooth versus bursty serves to organize EE events on the basis of several intrinsic and location parameters.

5.2. Intrinsic Event Characteristics and Locations

Histograms of maximum signal-to-noise ratio (or event size) and duration for events recorded during 12-h and 8-h orbits are shown in Figures 8 and 9, respectively. The histograms of event sizes (Figures 8a and 9a) follow a power law for both mission phases and event types. The power law distribution is steeper and the dynamic range in $S_{S/N}$ is smaller for smooth events (a factor of 20 in range) than for bursty events (factor of 400). Slightly more large events are seen for the 8-h orbits, but this difference is likely due to the longer observing time in that orbit. The power law indices are slightly larger for the 8-h orbits than for the 12-h orbits.

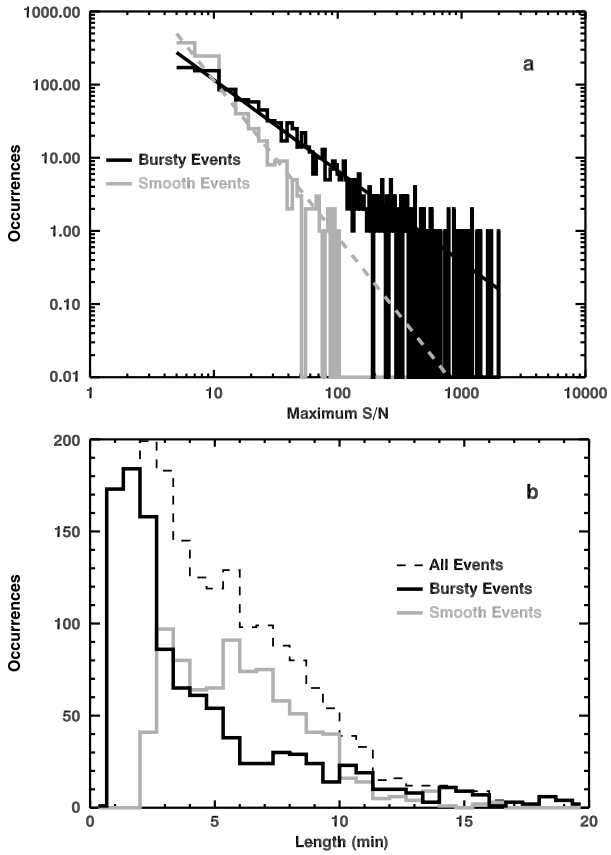

Figure 9. (a) Histograms of maximum $S_{S/N}$ values for EE events from the 8-h orbits for smooth events (gray) and bursty events (black). Power laws fit to the two profiles are shown. The scale, *a*, and power law index, *b*, respectively, are $a = 2040$ and $b = -1.2$ for bursty events and $a = 1.56 \times 10^4$ and $b = -2.1$ for smooth events. (b) Histograms of EE event durations from the 8-h orbits for smooth events (gray), bursty events (black), and all events (dashed).

The duration of most events is generally 15 min or less (Figures 8b and 9b), but some events last for almost 20 min. For both groups of orbits, there is a hint of a separate population of long events with durations from 15 to 20 min, but poor statistics preclude a definitive identification of such a population. The distribution of event durations for smooth events has a maximum between 5 and 10 min, whereas the bursty events tend to be shorter in duration. This effect is likely due, in part, to the inability of the smoothing parameters (equations (2) and (3)) to robustly delineate smooth versus bursty events for timescales within a few time steps of the baseline 20-s accumulation interval.

EE events are found to occur in distinct locations around Mercury as organized by local time, latitude, and altitude. A summary of EE event locations is given in Figure 10. The EE events are divided in the figure by orbit period and by bursty versus smooth character. It should be noted that the eccentric MESSENGER orbit does not traverse all portions of latitude-altitude phase space. As a consequence, latitude and altitude are not generally independent parameters when identifying EE event locations. Ninety-nine percent of all EE events have been seen at altitudes less than ~6000 km.

For the 12-h orbits, there is a clear dichotomy between bursty and smooth events. Bursty events are most often seen at higher latitudes than smooth events. Bursty events are also seen at all local times but are concentrated toward dawn and early morning local times. In contrast, smooth events are seen at lower latitudes and within a narrower range of latitudes than bursty events. As with the bursty events, smooth events are seen at all local times, but in contrast to bursty events, smooth events are concentrated at local times ranging from afternoon to dusk.

For the 8-h orbits, the dichotomy between bursty and smooth events is qualitatively similar to that seen for the 12-h orbits. However, in detail there are noteworthy differences between events recorded with the two orbit periods.

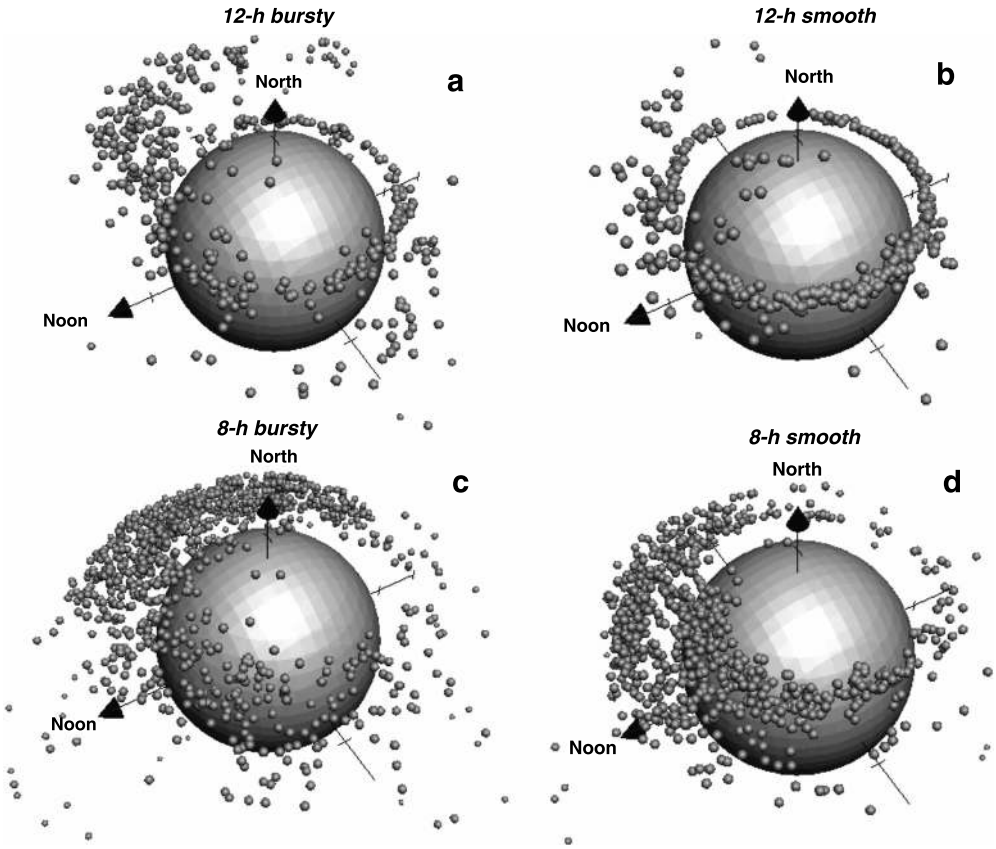

Figure 10. Geographic locations of EE events around Mercury in latitude, altitude, and local time separated by orbit period and event classification. The relative position of Mercury is shown by the gray globe; local time gives the azimuthal position around Mercury with respect to the Sun, with noon toward the left; north is up. (a and b) EE events from 12-h orbits; (c and d) EE events from 8-h orbits. Bursty events are shown in Figures 10a and 10c; smooth events are shown in Figures 10b and 10d.

The bursty events show a more continuous range of latitudes and a stronger preference for postmidnight to early morning local times. In contrast to the 12-h orbits, very few bursty events have been seen near midnight for the 8-h orbits. Smooth events seen during the 8-h orbits also show a wider and more continuous range of latitudes than for the 12-h orbits. Smooth event locations clearly are peaked at noon for the 8-h orbits compared with afternoon dusk local times for the 12-h orbits. As with the bursty events seen in 8-h orbits, but in contrast to the smooth events seen in 12-h orbits, very few smooth events are seen near midnight in the 8-h orbits.

These differences between events seen in the 12- and 8-h orbits are not fully understood, but it is likely that the full extent of EE event locations is not yet mapped because of the limited spatial sampling by the MESSENGER trajectory. Nevertheless, these data suggest that although Mercury does not have permanent radiation belts [see *Baker et al.*, 1986], the locations of the EE events do appear to form what can be termed "quasi-permanent structures." Here, the terms "permanent" and "structures" are used because the EE events occur in defined locations with reasonably clear boundaries that persist over time. The modifier "quasi" is added because the specific occurrence of any EE event is stochastic in nature and therefore introduces a component of unpredictability to EE event locations.

5.3. EE Events and Mercury's Magnetic Field

The physical mechanisms that drive EE events are almost certainly related to processes that take place in Mercury's dynamic magnetosphere [e.g., *Baker et al.*, 1986, 1987; *Slavin et al.*, 2010]. Therefore, to gain insight into EE event systematics and ultimately the underlying physical processes, we have binned the EE event occurrences and associated physical quantities by invariant latitude and magnetic local time (MLT). Invariant latitude [*Korth et al.*, 2014] is the latitude at which a magnetic field line threading the observation point maps onto a sphere of radius R_M (where R_M is Mercury's radius) centered on Mercury's offset dipole [*Anderson et al.*,

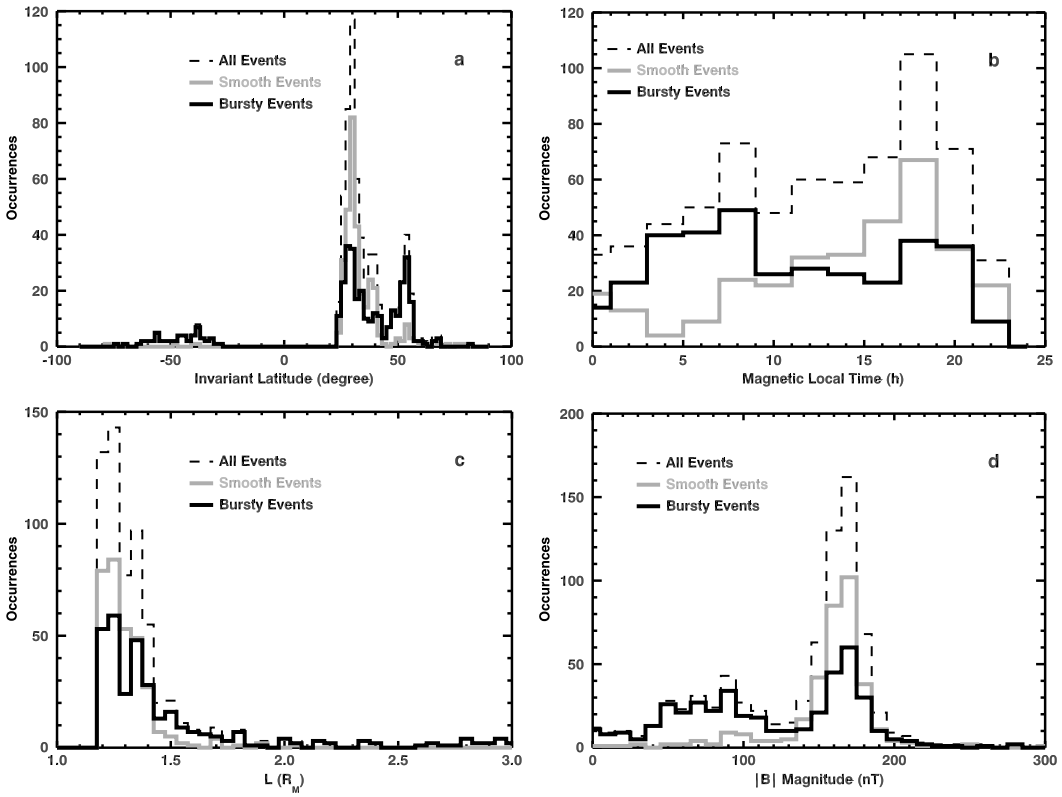

Figure 11. Histograms of EE events from 12-h orbits for parameters associated with Mercury's magnetic field: (a) invariant latitude; (b) magnetic local time; (c) *L* value; and (d) magnetic field magnitude *B*. In each panel, occurrences are separated into bursty (black), smooth (gray), and all events (dashed line).

2011]. Magnetic local time is the local time of the EE event location in Mercury solar magnetospheric (MSM) coordinates [*Korth et al*., 2014]. The MSM coordinate system is based on the Mercury solar orbital coordinate system (for which +*X* points toward the Sun, +*Y* toward dusk, and +*Z* toward north) but includes a 479 km offset in the +*Z* direction. The values of invariant latitude and MLT are derived from the magnetic field model of *Alexeev et al*. [2010] with parameters determined by *Johnson et al*. [2012]. Two additional parameters include the local magnetic field *L* values [*McIlwain*, 1961] and the magnetic field magnitude *B*, where *L* defines an axisymmetric surface of those lines of magnetic force from the dipole component of Mercury's internal field that intersect the magnetic equator at a distance *L* R_M from the dipole center.

Histograms of EE event locations binned by these four parameters for 12- and 8-h orbits are shown in Figures 11 and 12, respectively. Figures 11a and 12a display event locations as a function of invariant latitude and show information similar to that given in the three-dimensional mapping of Figure 10. For the 12-h orbits, event locations are restricted to a narrow latitude range mostly in the northern hemisphere. In particular, smooth events are peaked at 30°N invariant latitude, whereas bursty events are observed over a larger range of invariant latitude. For the 8-h orbits, the invariant latitude locations have a broader distribution than for the 12-h orbits, with a sizeable fraction of bursty events occurring in the southern hemisphere in MSM coordinates. In addition, smooth events are slightly concentrated toward more northern latitudes than bursty events in the observations from 8 h orbits.

MLT locations, shown in Figures 11b and 12b, clearly delineate the bursty versus smooth behavior initially seen in Figure 10. For both orbit periods, bursty events were most likely to occur near dawn and predawn local times. However, bursty events were more strongly peaked for predawn local times during 8-h orbits than for the 12-h orbits. Smooth events were dominantly located near afternoon for 12-h orbits and at noon for the 8-h orbits.

Histograms of event locations binned by *L* value and *B* (Figures 11c and 11d versus Figures 12c and 12d, respectively) also show clear systematic differences between bursty and smooth events. Bursty events occur across a wider range of *L* values than smooth events. In addition, bursty events have a wider dynamic range of

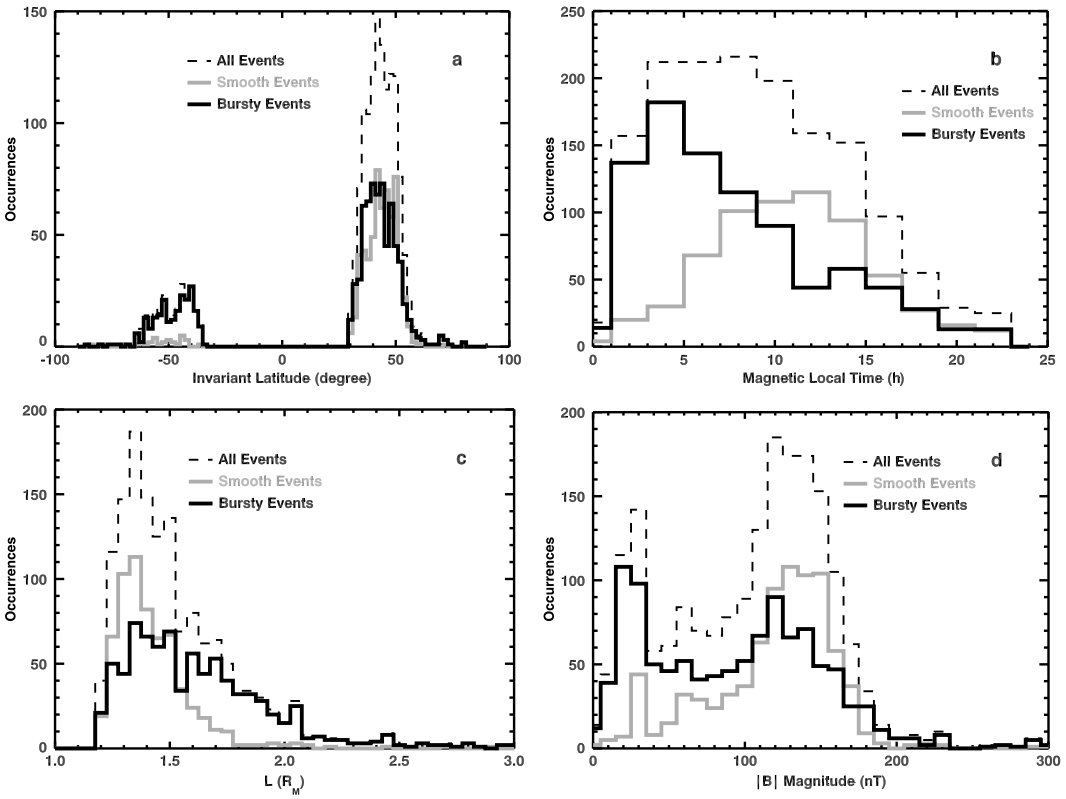

Figure 12. Histograms of EE events from 8-h orbits for parameters associated with Mercury's magnetic field: (a) invariant latitude; (b) magnetic local time; (c) *L* value; and (d) magnetic field magnitude *B*. In each panel, occurrences are separated into bursty (black), smooth (gray), and all events (dashed line).

L values for the 8-h orbits than for the 12-h orbits. Finally, *B* values for smooth events are peaked in the range ~130–160 nT for both orbit periods, whereas bursty events were observed with a wider range of *B* values (~10–200 nT). This pattern is consistent with the observation of more bursty events than smooth events at lower latitudes, as well as in the southern hemisphere where the field is much weaker at higher spacecraft altitudes in MESSENGER's orbit.

These data support the idea presented in section 5.2 that EE event locations have reasonably well-defined boundaries that persist in time. In addition, the differences with orbit period seen in Figure 10 are also seen

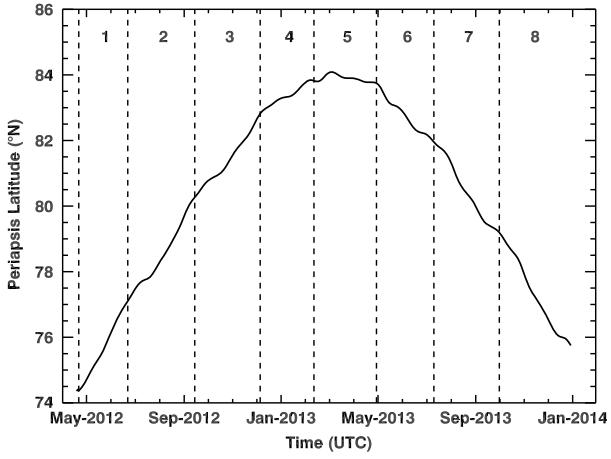

Figure 13. MESSENGER spacecraft periapsis latitude as a function of time for the 8-h orbits. Vertical dashed lines show eight different time bins used in Figure 14.

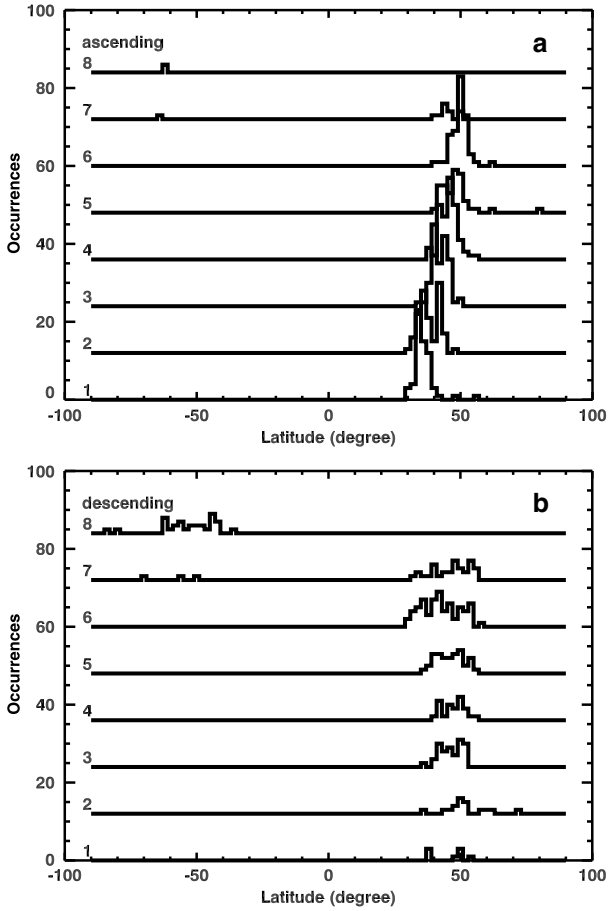

Figure 14. Histograms of the invariant latitude for smooth events measured from 8-h orbits and divided into the time bins shown in Figure 13. For the sake of clarity, the histograms are offset vertically. (a) Ascending portions of the orbits and (b) descending portions.

here. To provide some clues regarding the dependence on orbit period, we note the clear difference between the variation with invariant latitude for smooth events, for which the 12 h orbits show a highly peaked distribution at 30°N, and that for the 8 h orbits, which have a broader distribution ranging from 30°N to 60°N. A possible explanation for some of the difference with orbit period is that for the 8-h orbits that the MESSENGER spacecraft traveled through a different volume of MSM phase space than for the 12-h orbits.

Spacecraft periapsis latitude varied through the 8-h orbits considered in this study (Figure 13), and we use this quantity as a metric to illustrate how the 8-h orbit evolved. The orbit periapsis slowly moved northward and then southward, and therefore each orbit cut through a different portion of Mercury's magnetosphere. Figure 14 shows histograms of invariant latitude of smooth events for eight time bins through the interval of 8 h orbits studied here, further subdivided into ascending and descending orbit legs. Figure 14 shows a systematic behavior for the ascending legs characterized by a narrowly peaked distribution for which the latitude of the peak slowly varied from ~35°N to ~50°N. The distribution width for each time bin is similar in magnitude to the width for the full data set from 12-h orbits (Figure 11a). In contrast, for the descending legs, the latitude distribution progressively broadened and then switched to southern latitudes at the later times. To ensure that this behavior is not an artifact of the *Alexeev et al.* [2010] magnetic field model, we carried out a similar analysis with a Tsyganenko-type magnetic field model [*Tsyganenko*, 2002] and found the same qualitative results as those shown in Figure 14. Although a detailed description of the temporal behavior of EE events during the 8-h orbits is beyond the scope of the present survey, we interpret this initial look at the evolution of EE events with orbit geometry to indicate that as the spacecraft traveled through different portions of MSM phase space, the NS observed different aspects of the quasi-permanent structure for EE events.

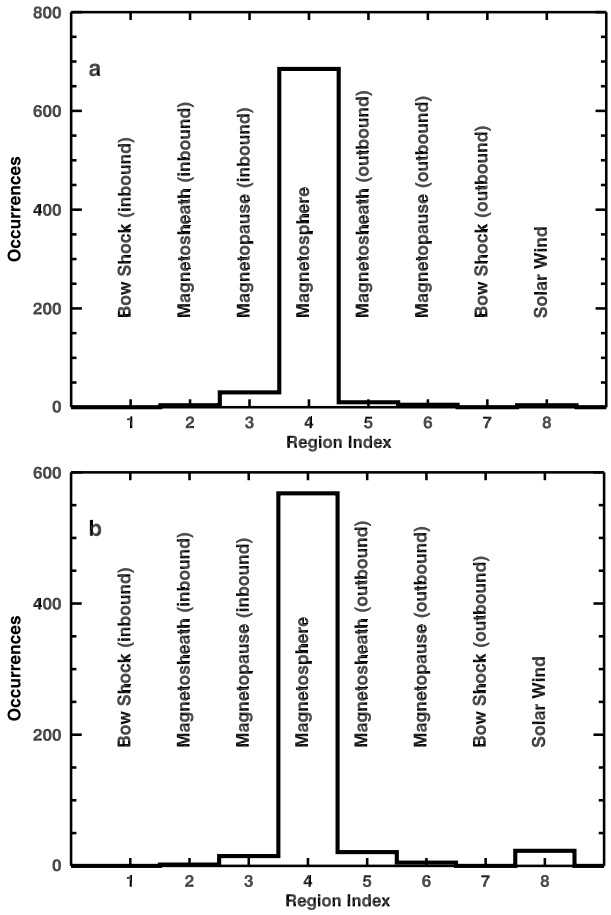

Figure 15. Histogram of NS-measured EE events by location relative to Mercury's magnetosphere. (a) From the 12-h orbits and (b) from approximately the first half of the 8-h orbits. Regions are identified by both region number (Figure 13) and inbound and outbound crossings of magnetospheric boundaries.

An important aspect of EE events is to know if they occur inside or outside Mercury's magnetosphere. Using criteria developed by *Anderson et al*. [2012], *Johnson et al*. [2012], and *Winslow et al*. [2013] to identify the magnetopause and bow shock crossings from MESSENGER magnetic field data, the locations of individual EE events from the 12-h orbits and approximately the first half of the 8-h orbits were identified with respect to these magnetospheric boundaries. For both the 12-h (Figure 15a) and 8-h (Figure 15b) orbits, EE events were overwhelmingly (~90%) located within Mercury's magnetosphere.

Another way to document the spatial distribution of the EE events is through event maps in two dimensions. Figures 16 and 17 show EE event locations mapped versus invariant latitude and local time; Figures 18 and 19 show EE event locations mapped versus *L* and *B*. Both sets of maps divide the data into the standard bursty versus smooth characterizations and 12-h versus 8-h orbits.

The maps in invariant latitude versus MLT (Figures 16 and 17) provide information on EE event locations with respect to the boundaries between the average locations of closed and open magnetic field lines. We obtained the average location of this boundary with the *Alexeev et al*. [2010] global magnetic field model using several modifications to the best-fit parameters determined by *Johnson et al*. [2012]. The tail current-sheet thickness was adjusted from the best-fit value of 0.09 R_M to 0.75 R_M to prevent mapping artifacts from magnetic islands arising from the discontinuity in the magnetic field at the inner edge of the current sheet. This modification was discussed in detail by *Korth et al*. [2014] and preserves the fidelity of the mapping to low altitudes to within a few degrees of latitude.

Some of the features discussed above are further illustrated by the data shown in Figures 16 and 17. First, this representation of EE event locations clearly shows that the vast majority of EE events occur within the closed

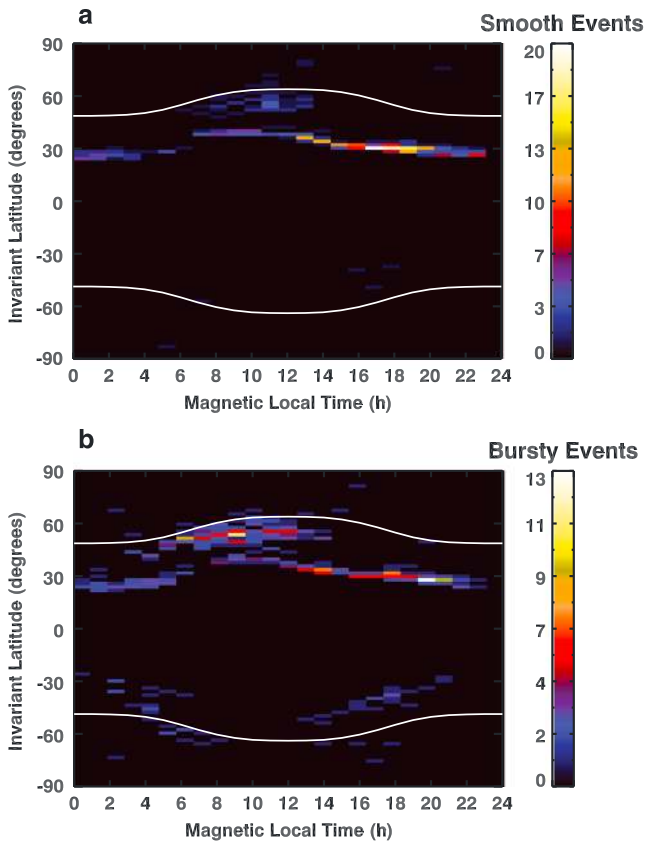

Figure 16. Map of EE event locations binned by magnetic local time and invariant latitude for observations from 12-h orbits. Color bar indicates number of events per bin. The white lines show the modeled boundary between open magnetic field lines at higher latitudes and closed field lines at lower latitudes. (a) Smooth events and (b) bursty events.

(equatorward) field-line region of Mercury's magnetosphere. Second, although EE event locations generally follow the shape of the boundary between open and closed field lines, there is a slight offset to earlier local times. We note that there are few such events at higher latitudes, which implies that the events are not related to cusp processes, even though high-energy electrons have been observed in Earth's cusps [*Sheldon et al.*, 1998]. Finally, the bursty versus smooth dichotomy is illustrated, whereby bursty events are more likely to occur near the boundary between open and closed field lines whereas smooth events are almost always well inside the boundary.

Maps of EE event by *L* versus *B* are shown in Figures 18 and 19. As originally laid out by *McIlwain* [1961], *L* versus *B* space provides a natural coordinate system that organizes magnetospheric phenomena. For example, the locations of Earth's radiation belts are well mapped as constant contours in this space. The *L* versus *B* maps for EE events do show some localization, in that smooth events generally show a narrower dynamic range than bursty events, and events from the 12-h orbits show a narrower dynamic range than events from the 8-h orbits. However, the highly localized, curved contours seen within Earth's magnetosphere [*McIlwain*, 1961] for locations of charged particles are not seen for EE event locations at Mercury. This observation reinforces a previous conclusion that Mercury's EE events do not resemble and do not constitute radiation belts [*Simpson et al.*, 1974; *Ho et al.*, 2012].

A final comparison of EE events with magnetospheric parameters involves EE event durations and sizes compared with the level of external solar forcing as quantified by a magnetic disturbance parameter that measures the magnetic variability in Mercury's magnetosphere [*Anderson et al.*, 2013; *Baker et al.*, 2013]. This disturbance parameter is determined by computing magnetic field fluctuations in three time-period bands of 0.1–2 s, 2–20 s, and 20–300 s. The values used here incorporate the fluctuation levels in all three bands and are ranked as percentiles. Figure 20 shows EE event length and maximum size versus magnetic disturbance for

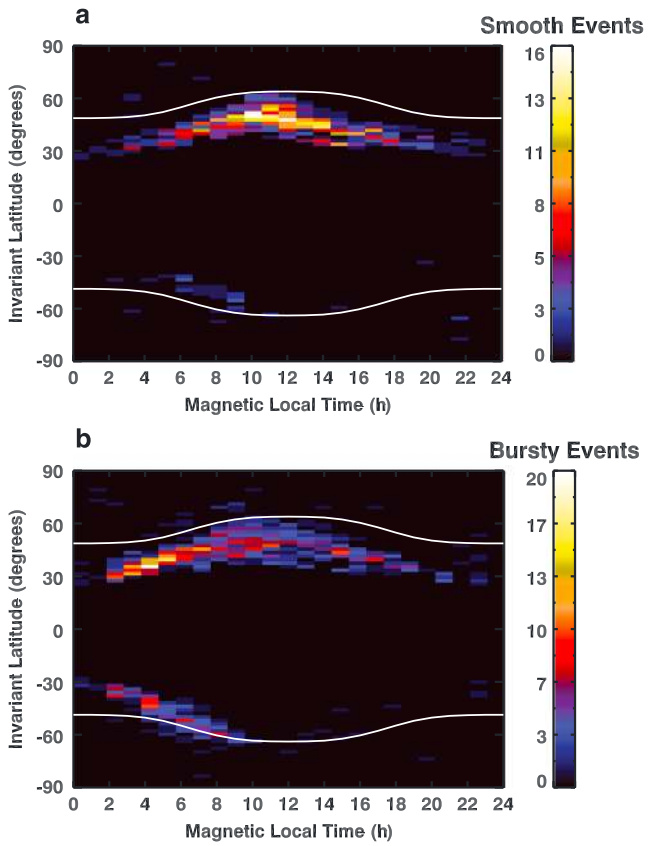

Figure 17. Map of EE event locations binned by magnetic local time and invariant latitude for observations from 8-h orbits. Color bar indicates number of events per bin. The white lines show the modeled boundary between open magnetic field lines at higher latitudes and closed field lines at lower latitudes. (a) Smooth events and (b) bursty events.

both 12- and 8-h orbits. These plots show that both of these EE event parameters are correlated with disturbance level and that EE events tend to be shorter and more intense under more disturbed conditions.

5.4. Temporal Behavior of EE Events

A key characteristic of EE events is the presence or absence of distinct periodicities within individual events. The initial report of energetic particles within Mercury's magnetosphere from Mariner 10 noted count-rate periodicities of ~5 to 6 s [*Simpson et al.*, 1974; *Eraker and Simpson*, 1986]. The observation and quantification of such periodicities can reveal information about characteristic timescales for particle acceleration processes within Mercury's magnetosphere. With the large NS data set and sub-5-s time resolution (section 2), the temporal variation of EE events can now be investigated in more detail. Figure 21a shows the time series of the bursty EE event from 22 May 2013 that is also shown in Figure 1f. This event was sufficiently intense to trigger the NS burst mode, so a full set of 1-s data is available for its duration. Inspection of these count-rate data shows clear episodic behavior with multiple frequencies ranging in period from tens of seconds to minutes.

The periodic behavior of the 1-s burst mode data is illustrated in Figure 21b by power spectral density (PSD) values versus period determined from the algorithms of *Scargle* [1982] and *Press and Rybicki* [1989]. The period values range from 2 to ~500 s; the larger value is the full event duration. As seen, the maximum power is found at a period of ~75 s, multiple higher-frequency modes are evident at periods between a few seconds and tens of seconds, and some power is seen at periods greater than 100 s. In contrast to this bursty event with strong periodic behavior, Figure 22 shows a PSD profile of the 1 April 2011 smooth event that is shown in Figures 1d and 3. This event shows little periodicity and most power at the longest time period.

High-time-cadence GRS measurements of EE events, which began on 25 February 2013, monitor the total count rate in the detector at 10-ms-long increments. Figure 23 details the 22 May 2013 bursty EE event as

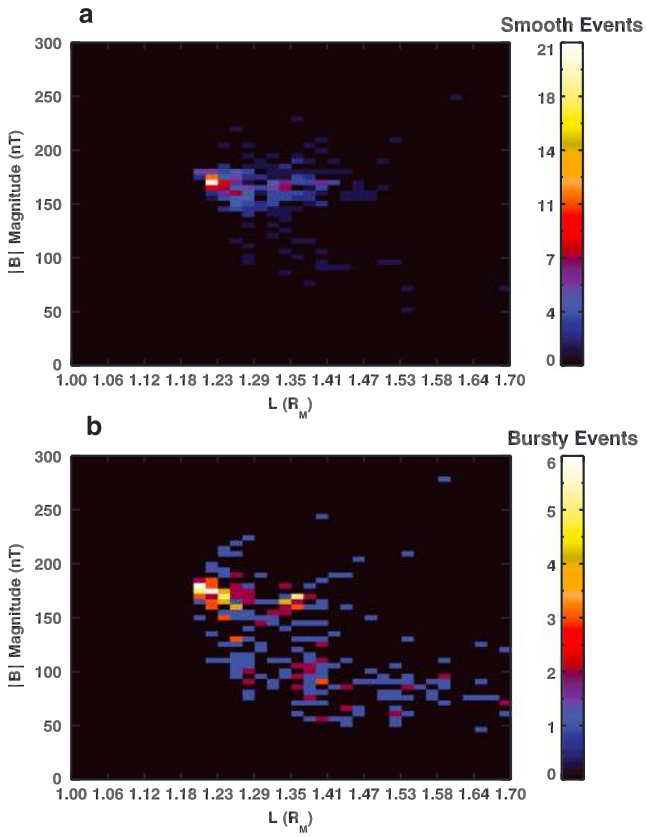

Figure 18. Map of EE event locations binned by *L* value and *B* for observations from 12-h orbits. Color bar indicates number of events per bin. (a) Smooth events and (b) bursty events.

observed by the GRS. The GRS data show the same structure as the NS burst-mode measurements for this event (Figure 21a), with minor differences that are attributable to differences in the instruments. In particular, the larger size of the GRS shield makes it more sensitive to lower-intensity EE events than the NS, but GRS event processing saturates at lower count rates (per unit area) than for the NS, reducing the relative intensity of the highest-count-rate portions of the EE events.

With the same algorithms as those used for the NS burst-mode data (Figures 21b and 22), PSD profiles of the 10-ms ACS data were calculated. The results (Figure 24) show periodic structure ranging from ~100 s down to tens of milliseconds. In the period range 1 to ~200 s (Figure 24a), the spectra are nearly identical to those observed by the NS (Figure 21b), with the observed difference again being attributable to the differences in instrument responses. Figures 24b and 24c show the PSD at higher frequencies and reveal structure at time intervals shorter than the sensitivity of the NS and Mariner 10 measurements. Periodicity is observed down to the cadence of the GRS measurements, indicating that even 10-ms data may not reveal the finest time structure of the EE events.

Analysis of additional events shows similar periodicities with a variety of spectral shapes. A detailed investigation of these parameters is beyond the scope of this study, but a few inferences can be made immediately. First, the periodicity originally reported by *Simpson et al*. [1974] is well within the range of periodicities observed with the NS data, and thus it is likely that the events observed in the Mariner 10 data were similar to the bursty events reported here. Second, the periods of 1 to 2 min displaying high power for the 22 May 2013 event (and other events) are similar in magnitude to the few-minute duration of tail-loading and tail-unloading events and the ~2 min Dungey cycle time for Mercury's magnetosphere [*Slavin et al*., 2010]. The Dungey cycle governs the characteristic timescale for the circulation of magnetic flux from the location of subsolar reconnection to the magnetotail and then back to the dayside magnetosphere. Particles tied to the magnetic field lines will follow this motion from the dayside over the polar caps to the nightside and from the

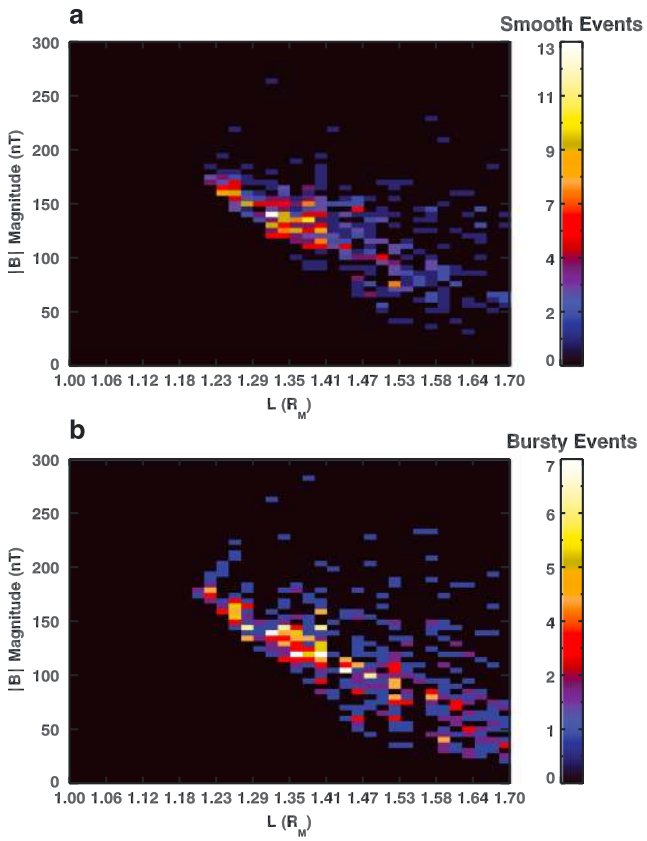

Figure 19. Map of EE event locations by *L* value and *B* for observations from 8-h orbits. Color bar indicates number of events per bin. (a) Smooth events and (b) bursty events.

northern and southern magnetotail lobes toward the cross-tail current sheet. This similarity between EE event periodicities and timescales for tail-loading and tail-unloading events, which *Slavin et al.* [2010] linked to substorm events [*Baker et al.*, 1987, 1996], suggests that some portion of the EE events are also related or linked to substorm events. Since the particle bounce times from north to south will be shorter than a few minutes, the higher-frequency portions of the spectra seen here could be related to north-south mirroring processes.

6. Comparison of NS With XRS and EPS

To complete this survey of NS-measured EE events, it is useful to compare the NS data with other measures of EE events, namely, data from the MESSENGER EPS and XRS. The initial identification of EE events from the MESSENGER mission was made from EPS measurements, as reported by *Ho et al.* [2011a, 2011b, 2012]. The most current listing of EPS-measured EE events is from 12-h orbits between 27 March 2011 and 22 March 2012. During this interval, 7% (51 events) of the set of events identified by the NS (733 events) were also seen on the EPS. The substantially larger number of NS-measured events is mostly due to the fact that the NS has a detector area (100 cm^2) [*Goldsten et al.*, 2007] more than two orders of magnitude larger than the EPS detector area (40 mm^2) [*Andrews et al.*, 2007].

To further compare the two data sets, the NS data were searched for time correspondences with EPS-identified events. This search was conducted by choosing a time window, $\Delta\tau$, centered on NS midpoint detection times. The size of this window was varied from 5 to 80 min, and the number of EPS events within the window was tallied. Figure 25a shows the results of this analysis as a plot of the EPS fraction (i.e., the fraction of NS events that are also logged as an EPS event) versus $\Delta\tau$. Triangles show the fraction for a single EPS event within the window, diamonds show the fraction for cases when two EPS events occur within the window, and circles show the sum of one, two, or more EPS events within the window. For short $\Delta\tau$ values, the EPS fraction is small (0.01); the fraction rises for longer time windows and tends to plateau around $\Delta\tau = 40$ min, which is

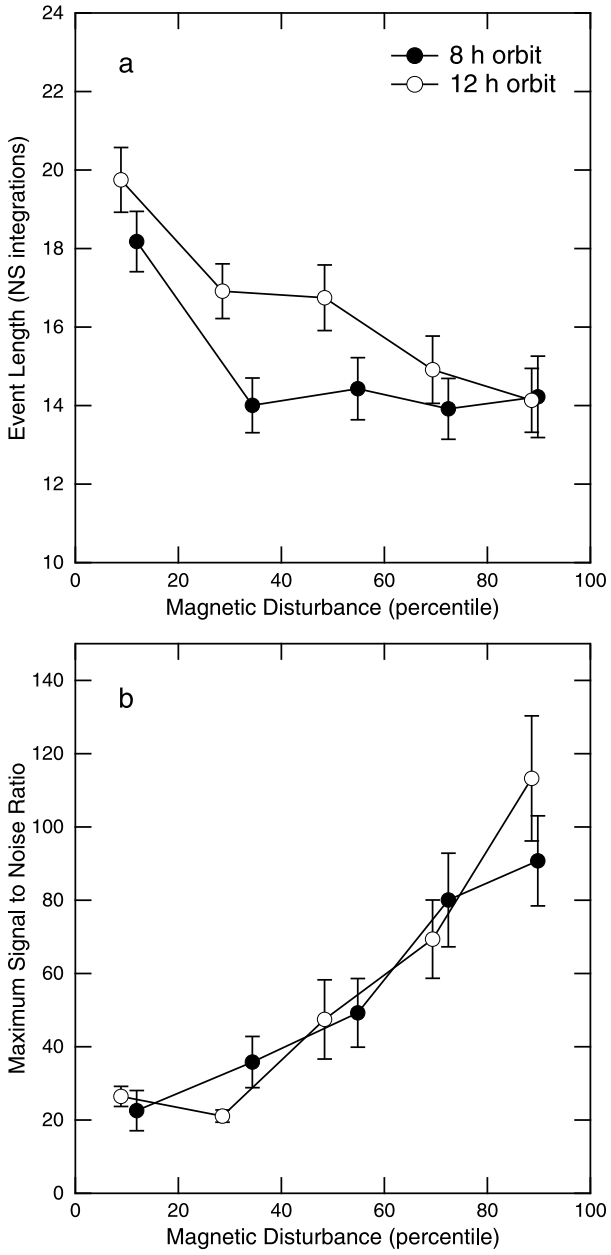

Figure 20. (a) EE event durations and (b) maximum $S_{S/N}$ values plotted versus magnetic disturbance for observations form 12-h (open circles) and 8-h (filled circles) orbits.

approximately the time during a given orbit when the spacecraft passes close to Mercury. Figures 25b and 25c show histograms of event sizes for the full EPS and NS data sets and the fraction of overlapping events for $\Delta\tau = 40$ min. Figure 25b shows that just over half of the EPS events (51%) were also seen by the NS within the 40 min time window. Given that the duration of NS-measured EE events is always less than 20 min (Figures 8 and 9), this result suggests that the NS and EPS are responding to distinct EE occurrences. Further, fewer than 4% of the NS events are seen by the EPS, and none of the largest NS events were seen by the EPS. These results suggest that the NS and EPS generally respond to different populations of energetic particles. This lack of correspondence between the NS and EPS data is not fully understood, but in addition to the substantial difference in detector sizes, it is possible that a further reason for the lack of correspondence between the two data sets is that the EPS has a highly directional response whereas the NS has a more isotropic response and is sensitive to a wider range of events.

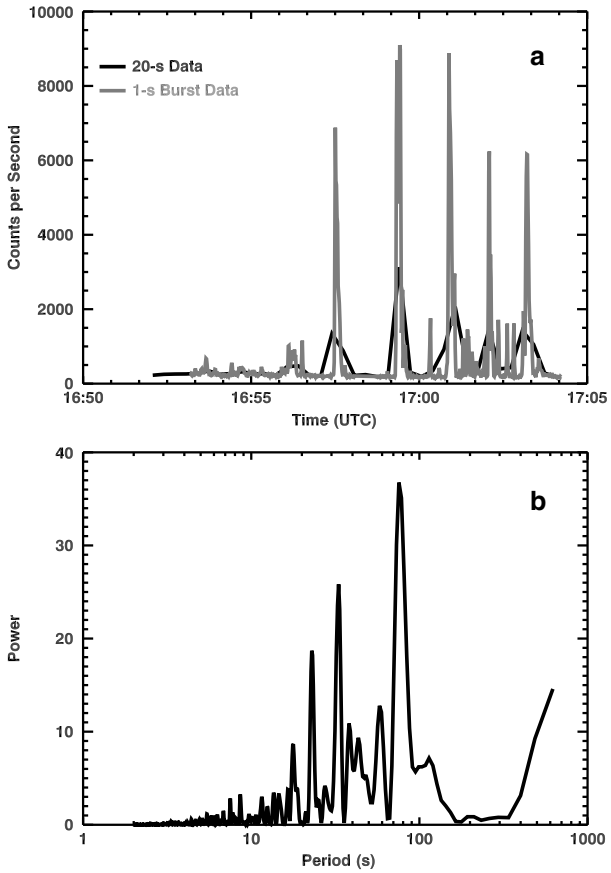

Figure 21. (a) Low-energy count-rate data from the NS BP scintillator for the 22 May 2013 EE event. The 20-s accumulation data are shown in black; 1-s burst-mode data are shown in gray. (b) Power spectral density of the 1-s burst-mode data from Figure 21a.

As described by *Ho et al*. [2011b], the XRS is also sensitive to EE events. A database of XRS-measured EE events has been compiled for dates ranging from 4 April 2011 to mid-January 2014. This database was developed with an algorithm that incorporates the XRS counting rate, the spectral index, the count-rate difference between the filtered and unfiltered sensors, and the location of the events. During the times of overlap with the NS data taken from 10 April 2011 to 31 December 2013, there are 2083 XRS EE events and 2677 NS EE

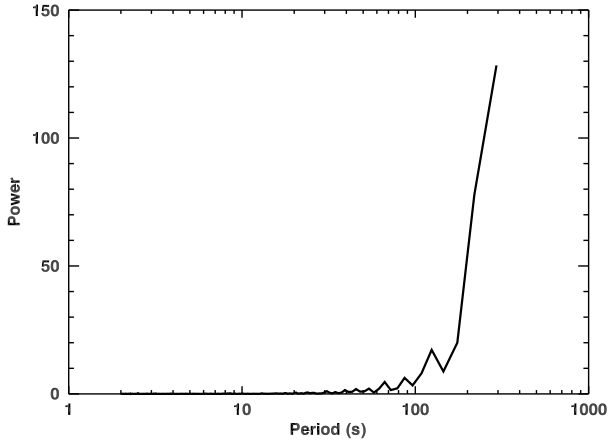

Figure 22. Power spectral density of the time series for the 1 April 2011 EE event from Figure 3.

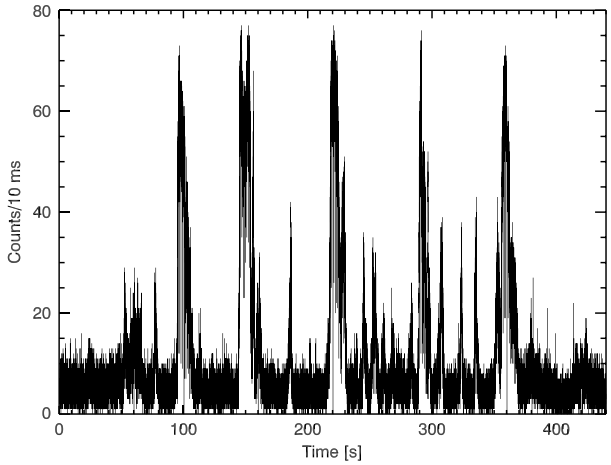

Figure 23. Time series of the 22 May 2013 EE event from Figure 21 as observed by the GRS ACS at 10-ms resolution.

events, so the NS has identified approximately 20% more events than the XRS. Two aspects of the XRS data deserve to be noted. First, a detailed study of the XRS EE event detection algorithm for small events was not carried out. Thus, some fraction of small events from the XRS might be missed with the current algorithm. Second, some large events are missed in the XRS data because the XRS sensor can enter a safe mode, when the sensor is turned off to protect the front-end electronics from high fluxes of charged particles.

A time-correspondence analysis was carried out for the XRS data in a manner similar to the analysis of EPS data. Figure 26a shows that the optimum time window for the XRS-NS comparison is close to 40 min, but with a flatter plateau than for the EPS data. Figures 26b and 26c show histograms of event sizes from both the XRS and NS data that include the total data sets as well as events seen within a $\Delta\tau = 40$ min time window. In both cases, approximately 50–55% of the events seen in one data set were seen in the other. In contrast to the NS-EPS comparison, both the NS and XRS detect the largest events. Differences between the NS and XRS increase as event size decreases. These results suggest that, especially for the largest EE events, the NS and XRS are responding to the same or similar population of energetic electrons. For smaller events, differences in absolute detection sensitivity, angular response, and/or the XRS EE event detection algorithm may all contribute to differences in event detection. Finally, a comparison of the XRS and NS size histograms shows that the XRS data turn over for the smallest event sizes whereas the NS data follow a uniform power law down

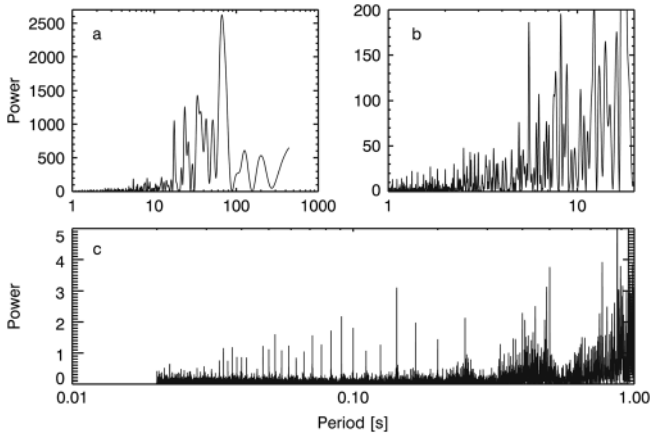

Figure 24. Power spectral density (PSD) for the 22 May 2013 EE event as measured by the GRS ACS. (a) The PSD in the 1–1000 s period range is a close match to the spectra from the NS (Figure 21b). (b and c) The PSD at shorter periods shows that periodic structure continues for this event at higher frequencies than those sampled by the NS. Periodicity appears to the very limit of the measurements (0.02 s), suggesting that even the 10-ms-long GRS ACS measurements do not sample the highest frequencies present in EE events.

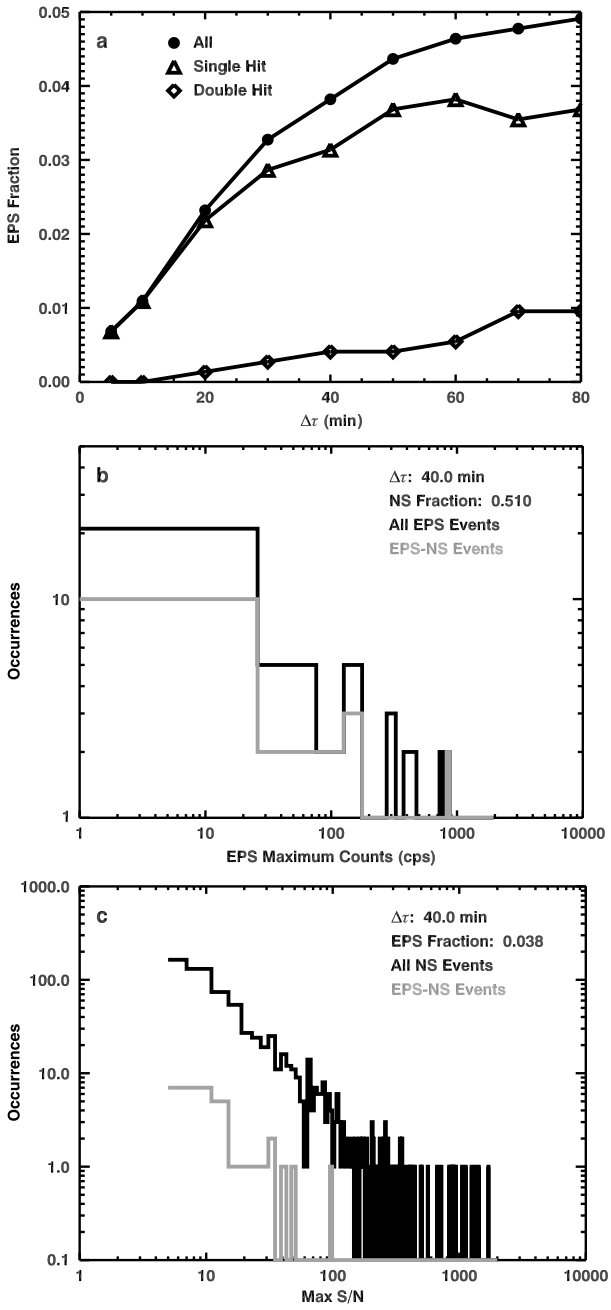

Figure 25. Comparison of EE events measured with the NS and EPS. (a) Fraction of NS-measured EE events that are also seen with the EPS as a function of the time window $\Delta\tau$ selected to represent the NS-measured event. Triangles show the fraction of NS-measured events with a single EPS-measured EE event, diamonds show the fraction of NS-measured events with two EPS-measured EE events, and filled circles show the total number of events seen in both data sets. (b) Histograms of maximum count rates for EPS-measured events; the black trace shows all EPS events, and the gray trace shows EPS events that correspond to an NS event for a $\Delta\tau$ value of 40 min. (c) Histograms of maximum $S_{S/N}$ values for NS-measured events; the black trace shows all NS events, and the gray trace shows NS events that correspond to an EPS event for a $\Delta\tau$ value of 40 min.

to the smallest event sizes. This observation suggests that the XRS has a limit in sensitivity and/or there are no events smaller than its lowest detected intensity. In contrast, the uniform power law of the NS data suggests that the NS is fully sensitive even to the smallest events it detects. Given that the dynamic range in intensity of events detected by the NS is larger (nearly three orders of magnitude) than that for the XRS (two orders of

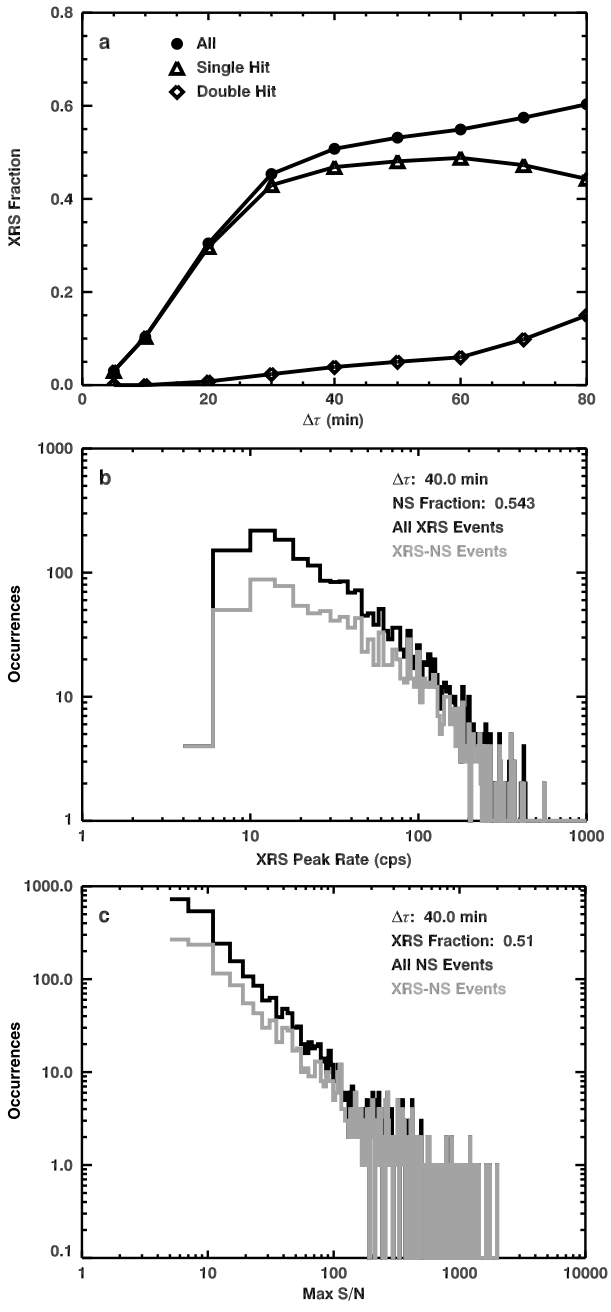

Figure 26. Comparison of EE events measured with the NS and XRS. (a) Fraction of NS-measured EE events that are also seen with the XRS as a function of the time window $\Delta\tau$ selected to represent the NS-measured event. Triangles show the fraction of NS-measured events with a single XRS-measured EE event, diamonds show the fraction of NS-measured events with two XRS-measured EE events, and filled circles show the total number of events seen in both data sets. (b) Histograms of maximum count rates for XRS-measured events; the black trace shows all XRS events, and the gray trace shows XRS events that correspond to an NS event for a $\Delta\tau$ value of 40 min. (c) Histograms of maximum $S_{S/N}$ values for NS-measured events; the black trace shows all NS events, and the gray trace shows NS events that correspond to an XRS event for a $\Delta\tau$ value of 40 min.

magnitude), it is more likely that the NS data capture the full range of intensities, and there may have been even smaller events not yet identified with the NS data.

7. Summary and Future Work

This study is the first comprehensive survey of EE events at Mercury and has resulted in a sample of 2711 EE events measured with the MESSENGER NS. With this survey, we have documented a number of important characteristics of EE events.

1. The sizes of EE events span a wide dynamic range (a factor of 400), and the distribution of events by size follows a power law. The duration of EE events ranges from tens of seconds to 15–20 min.
2. EE events can be classified within a continuous range of two end-member types, "bursty" and "smooth." These two types of events have distinct intrinsic properties and are observed to occur in different locations around Mercury. Because of these distinct characteristics, it is possible that different physical mechanisms are responsible for the bursty and smooth events. Further, the EE events identified from Mariner 10 data [*Simpson et al.*, 1974] were likely bursty events, because of their highly variable time behavior.
3. Almost all EE events are observed to occur within Mercury's magnetosphere on closed field lines, although bursty events are more likely to be seen near the boundaries between open and closed field lines than smooth events.
4. EE event locations plotted versus magnetic local time and invariant latitude form what we interpret as quasi-permanent structures. The term "permanent structure" refers to the observation that EE events occur in well-defined locations with clear boundaries that persist over time. The modifier "quasi" denotes the fact that EE event occurrence is intrinsically stochastic. These quasi-permanent structures show clear differences for bursty and smooth events. Bursty events occur closer to dawn and at high latitudes, whereas smooth events are seen most often near noon-to-dusk local times and at lower latitudes.

5. A subset of EE events displays strong periodicities with peaks in power at periods that range from tens of milliseconds to hundreds of seconds. These results are consistent with the reports from Mariner 10 observations of periodicities at a few seconds period [*Simpson et al*., 1974]. The peaks in power at periods of a few minutes are consistent with the Dungey-cycle timescale that has been linked to substorm events that originate in Mercury's magnetotail region [*Baker et al*., 1987; *Slavin et al*., 2010]. Power at higher frequencies may be related to phenomena such as north-south mirroring of the energetic electrons.

These results point to multiple areas for future study. First, more work is needed to understand the locations of EE events. Although EE events occur in well-defined locations that persist in time, the precise boundaries and extents of these quasi-permanent structures are still not well understood. In particular, we do not have a good explanation for the systematic variation of EE event locations with latitude and altitude. Our understanding of the three-dimensional distribution of EE events (local time, latitude, and altitude) can progress in multiple ways. There will be one and one quarter more years of EE event data by the time the MESSENGER mission ends in spring 2015. During that time, the spacecraft periapsis altitude will drop below 100 km and provide EE event coverage within a volume of altitude, latitude, and local time that has not yet been encountered. In addition to mapping EE events in a new portion of three-dimensional phase space, the systematic behavior of three-dimensional event locations should be investigated separately for bursty and smooth events to understand how their locations relate to the physical mechanisms that generate the events.

Second, detailed studies should be carried out to investigate and understand the periodic behavior that occurs within individual EE events using the high-time-resolution data from the NS burst mode and GRS ACS. Although a subset of events shows strong periodicities, the systematic behavior (if any) of these periodicities is not understood. Basic questions that can be asked include the following: Are there some locations where specific frequencies are present or absent? Does the periodic behavior of EE events change in response to forcing factors in the environment external to the magnetosphere, and, if so, how? Can north-south bounce periods be investigated with the NS and GRS ACS EE event data? Do these measurements provide additional evidence for particle loss at Mercury's surface associated with its asymmetric magnetic field, as suggested by *Korth et al*. [2014], and as shown with measurements of electron-induced X-ray fluorescence [*Starr et al*., 2012]?

A third area of study is to investigate possible nonisotropic behavior of EE events using multiple data sets from the MESSENGER instruments. Such a study is enabled by the facts that energetic electrons do not penetrate into spacecraft materials and that the different instruments that detect EE events have different view directions. Whereas both the NS and EPS are located on the back of the MESSENGER spacecraft, the NS has a large hemispherical field of view, and the EPS is restricted to a planar field of view of 160° by 12° [*Andrews et al*., 2007]. As a consequence, the NS and EPS are not sensitive to the same angular distribution of energetic electrons. Like the NS, the GRS ACS and XRS have relatively large viewing geometries, but they have a central look direction that is orthogonal to that of the NS. If the energetic electrons in EE events are not isotropic, then the detection sensitivity and/or event size would likely show relative differences among the four instruments. The initial comparison of NS, XRS, and EPS data given in section 6 suggests that such differences may indeed be present.

Finally, much progress can be made in understanding the physics behind EE events by selecting a small subset of events for case studies, in which all relevant data for each of the events (energetic particle, plasma, and magnetic field) are analyzed in full. Now that the broad outlines of EE events are mapped (e.g., size, duration, frequency, location, and classification type), specific events for such case studies can be readily selected to cover the wide range of EE event parameters.

Acknowledgments

The MESSENGER project is supported by the NASA Discovery Program under contracts NAS5-97271 to The Johns Hopkins University Applied Physics Laboratory and NASW-00002 to the Carnegie Institution of Washington. Several authors are supported by NASA's MESSENGER Participating Scientist Program. All original data reported in this paper are archived by the NASA Planetary Data System (http://pds-geosciences/wustl.edu/missions/messenger/index.htm).

Michael Liemohn thanks Theodore Fritz and another reviewer for their assistance in evaluating this paper.

References

Agostinelli, S., et al. (2003), GEANT4—A simulation toolkit, *Nucl. Instrum. Methods Phys. Res., Sect. A*, *506*, 250–303, doi:10.1016/S0168-9002(03)01368-8.

Alexeev, I. I., et al. (2010), Mercury's magnetospheric magnetic field after the first two MESSENGER flybys, *Icarus*, *209*, 23–39, doi:10.1016/j.icarus.2010.01.024.

Anderson, B. J., C. L. Johnson, H. Korth, M. E. Purucker, R. M. Winslow, J. A. Slavin, S. C. Solomon, R. L. McNutt Jr., J. M. Raines, and T. H. Zurbuchen (2011), The global magnetic field of Mercury from MESSENGER orbital observations, *Science*, *333*, 1859–1862, doi:10.1126/science.1211001.

Anderson, B. J., C. L. Johnson, H. Korth, R. M. Winslow, J. E. Borovsky, M. E. Purucker, J. A. Slavin, S. C. Solomon, M. T. Zuber, and R. L. McNutt Jr. (2012), Low-degree structure in Mercury's planetary magnetic field, *J. Geophys. Res.*, *117*, E00l12, doi:10.1029/2012JE004159.

Anderson, B. J., C. L. Johnson, and H. Korth (2013), A magnetic disturbance index for Mercury's magnetic field derived from MESSENGER Magnetometer data, *Geochem. Geophys. Geosyst.*, *14*, 3875–3886, doi:10.1002/ggge.20242.

Andrews, G. B., et al. (2007), The Energetic Particle and Plasma Spectrometer instrument on the MESSENGER spacecraft, *Space Sci. Rev.*, *131*, 523–556.

Armstrong, T. P., S. M. Krimigis, and L. J. Lanzerotti (1975), A reinterpretation of the reported energetic particle fluxes in the vicinity of Mercury, *J. Geophys. Res.*, *80*, 4015–4017, doi:10.1029/JA080i028p04015.

Baker, D. N., J. A. Simpson, and J. H. Eraker (1986), A model of impulsive acceleration and transport of energetic particles in Mercury's magnetosphere, *J. Geophys. Res.*, *91*, 8742–8748, doi:10.1029/JA091iA08p08742.

Baker, D. N., J. E. Borovsky, J. O. Burns, G. R. Gisler, and M. Zeilik (1987), Possible calorimetric effects at Mercury due to solar wind-magnetosphere interactions, *J. Geophys. Res.*, *92*, 4707–4712, doi:10.1029/JA092iA05p04707.

Baker, D. N., T. I. Pulkkinen, V. Angelopoulos, W. Baumjohann, and R. L. McPherron (1996), Neutral line model of substorms: Past results and present view, *J. Geophys. Res.*, *101*, 12,975–13,010, doi:10.1029/95JA03753.

Baker, D. N., et al. (2013), Solar wind forcing at Mercury: WSA-ENLIL model results, *J. Geophys. Res. Space Physics*, *118*, 45–57, doi:10.1029/2012JA018064.

Burks, M., C. P. Cork, D. Eckels, E. Hull, N. W. Madden, W. Miller, J. Goldsten, E. Rhodes, and B. Williams (2004), Thermal design and performance of the Gamma-Ray Spectrometer for the MESSENGER spacecraft, in *Proceedings of the IEEE Nuclear Science Symposium, 2004*, vol. 1, edited by J. A. Seibert, pp. 390–394, Institute of Electrical and Electronics Engineers, Piscataway, N. J.

Christon, S. P., J. Feynman, and J. A. Slavin (1987), Dynamic substorm injections: Similar magnetospheric phenomena at Earth and Mercury, in *Magnetotail Physics*, edited by A. T. Y. Lui, pp. 393–400, Johns Hopkins Univ. Press, Baltimore, Md.

Eraker, J. H., and J. A. Simpson (1986), Acceleration of charged particles in Mercury's magnetosphere, *J. Geophys. Res.*, *91*, 9973–9993, doi:10.1029/JA091iA09p09973.

Feldman, W. C., et al. (2010), Evidence for extended acceleration of solar flare ions from 1–8 MeV solar neutrons detected with the MESSENGER Neutron Spectrometer, *J. Geophys. Res.*, *115*, A01102, doi:10.1029/2009JA014535.

Goldsten, J. O., et al. (2007), The MESSENGER Gamma-Ray and Neutron Spectrometer, *Space Sci. Rev.*, *131*, 339–391, doi:10.1007/s11214-007-9262-7.

Ho, G. C., et al. (2011a), MESSENGER observations of transient bursts of energetic electrons in Mercury's magnetosphere, *Science*, *333*, 1865–1868.

Ho, G. C., R. D. Starr, R. E. Gold, S. M. Krimigis, J. A. Slavin, D. N. Baker, B. J. Anderson, R. L. McNutt Jr., L. R. Nittler, and S. C. Solomon (2011b), Observations of suprathermal electrons in Mercury's magnetosphere during the three MESSENGER flybys, *Planet. Space Sci.*, *59*, 2016–2025, doi:10.1016/j.pss.2011.01.011.

Ho, G. C., S. M. Krimigis, R. E. Gold, D. N. Baker, B. J. Anderson, H. Korth, J. A. Slavin, R. L. McNutt Jr., R. M. Winslow, and S. C. Solomon (2012), Spatial distribution and spectral characteristics of energetic electrons in Mercury's magnetosphere, *J. Geophys. Res.*, *117*, A00M04, doi:10.1029/2012JA017983.

Johnson, C. L., et al. (2012), MESSENGER observations of Mercury's magnetic field structure, *J. Geophys. Res.*, *117*, E00L14, doi:10.1029/JE004217.

Korth, H., B. J. Anderson, D. J. Gershman, J. M. Raines, J. A. Slavin, T. H. Zurbuchen, S. C. Solomon, and R. L. McNutt Jr. (2014), Plasma distribution in Mercury's magnetosphere derived from MESSENGER Magnetometer and Fast Imaging Plasma Spectrometer observations, *J. Geophys. Res. Space Physics*, *119*, 2917–2932, doi:10.1002/2013JA019567.

Lawrence, D. J., et al. (2013), Evidence for water ice near Mercury's north pole from MESSENGER Neutron Spectrometer measurements, *Science*, *339*, 292–296.

Leary, J. C., et al. (2007), The MESSENGER spacecraft, *Space Sci. Rev.*, *131*, 187–217.

Mazets, E. P., R. L. Aptekar, T. L. Cline, D. D. Frederiks, J. O. Goldsten, S. V. Golenetskii, K. Hurley, A. von Kienlin, and V. D. Pal'shin (2008), A giant flare from a soft gamma repeater in the Andromeda galaxy (M31), *Astrophys. J.*, *680*, 545–549, doi:10.1086/587955.

McIlwain, C. E. (1961), Coordinates for mapping the distribution of magnetically trapped particles, *J. Geophys. Res.*, *66*, 3681–3691, doi:10.1029/JZ066i011p03681.

Peplowski, P. N., et al. (2011), Radioactive elements on Mercury's surface from MESSENGER: Implications for the planet's formation and evolution, *Science*, *333*, 1850–1852.

Peplowski, P. N., E. A. Rhodes, D. K. Hamara, D. J. Lawrence, L. G. Evans, L. R. Nittler, and S. C. Solomon (2012), Variations in the abundances of potassium and thorium on the surface of Mercury: Results from the MESSENGER Gamma-Ray Spectrometer, *J. Geophys. Res.*, *117*, E00L04, doi:10.1029/2012JE004141.

Press, W. H., and G. B. Rybicki (1989), Fast algorithm for spectral analysis of unevenly sampled data, *Astrophys. J.*, *338*, 277–280.

Scargle, J. D. (1982), Studies in astronomical time-series analysis, II. Statistical aspects of spectral-analysis of unevenly spaced data, *Astrophys. J.*, *263*, 835–853.

Sheldon, R. B., H. E. Spence, J. D. Sullivan, T. A. Fritz, and J. Chen (1998), The discovery of trapped energetic electrons in the outer cusp, *Geophys. Res. Lett.*, *25*, 1825–1828, doi:10.1029/98GL01399.

Simpson, J. A., J. H. Eraker, J. E. Lamport, and P. H. Walpole (1974), Electrons and protons accelerated in Mercury's magnetic field, *Science*, *185*, 160–166.

Slavin, J. A., et al. (2010), MESSENGER observations of extreme loading and unloading of Mercury's magnetic tail, *Science*, *329*, 665–668.

Solomon, S. C., R. L. McNutt Jr., R. E. Gold, and D. L. Domingue (2007), MESSENGER mission overview, *Space Sci. Rev.*, *131*, 3–39, doi:10.1007/s11214-007-1175-9247-6.

Starr, R. D., D. Schriver, L. R. Nittler, S. Z. Weider, P. K. Byrne, G. C. Ho, E. A. Rhodes, C. E. Schlemm II, S. C. Solomon, and P. M. Travnicek (2012), MESSENGER detection of electron-induced X-ray fluorescence from Mercury's surface, *J. Geophys. Res.*, *117*, E00L02, doi:10.1029/2012JE004118.

Sundberg, T., et al. (2012), MESSENGER observations of dipolarization events in Mercury's magnetotail, *J. Geophys. Res.*, *117*, A00M03, doi:10.1029/2012JA017756.

Tsyganenko, N. A. (2002), A model of the near magnetosphere with a dawn-dusk asymmetry. 1. Mathematical structure, *J. Geophys. Res.*, *107*(A8), 1179, doi:10.1029/2001JA000219.

Winslow, R. M., B. J. Anderson, C. L. Johnson, J. A. Slavin, H. Korth, M. E. Purucker, D. N. Baker, and S. C. Solomon (2013), Mercury's magnetopause and bow shock from MESSENGER Magnetometer observations, *J. Geophys. Res. Space Physics*, *118*, 2213–2227, doi:10.1002/jgra.50237.